MATERIAL CHARACTERIZATION AT HIGH STRAIN RATES USING MODIFIED TAYLOR IMPACT TEST AND VELOCITY INTERFEROMETRY

A THESIS SUBMITTED TO
THE GRADUATE SCHOOL OF NATURAL AND APPLIED SCIENCES
OF
MIDDLE EAST TECHNICAL UNIVERSITY

BY

LATİF KESEMEN

IN PARTIAL FULFILLMENT OF THE REQUIREMENTS
FOR
THE DEGREE OF MASTER OF SCIENCE
IN
AEROSPACE ENGINEERING

SEPTEMBER 2016

Approval of the thesis:

MATERIAL CHARACTERIZATION AT HIGH STRAIN RATES USING MODIFIED TAYLOR IMPACT TEST AND VELOCITY INTERFEROMETRY

submitted by **LATİF KESEMEN** in partial fulfillment of the requirements for the degree of **Master of Science in Aerospace Engineering, Middle East Technical University by,**

Prof. Dr. Gülbin Dural Ünver _____
Dean, Graduate School of **Natural and Applied Sciences**

Prof. Dr. Ozan Tekinalp _____
Head of Department, **Aerospace Engineering**

Prof. Dr. Altan Kayran _____
Supervisor, **Aerospace Engineering Dept., METU**

Examining Committee Members:

Assoc. Prof. Dr. Demirkan Çöker _____
Aerospace Engineering Dept., METU

Prof. Dr. Altan Kayran _____
Aerospace Engineering Dept., METU

Asst. Prof. Dr. Ercan Gürses _____
Aerospace Engineering Dept., METU

Assoc. Prof. Dr. Yiğit Yazıcıoğlu _____
Mechanical Engineering Dept., METU

Prof. Dr. Nuri Durlu _____
Mechanical Engineering Dept., TOBB ETU

Date: **08.09.2016**

I hereby declare that all information in this document has been obtained and presented in accordance with academic rules and ethical conduct. I also declare that, as required by these rules and conduct, I have fully cited and referenced all material and results that are not original to this work.

Name, Last name : Latif Kesemen

Signature :

ABSTRACT

MATERIAL CHARACTERIZATION AT HIGH STRAIN RATES USING MODIFIED TAYLOR IMPACT TEST AND VELOCITY INTERFEROMETRY

Kesemen, Latif

M.Sc., Department of Aerospace Engineering

Supervisor : Prof. Dr. Altan Kayran

September 2016, 98 pages

Metallic materials in aerospace structures are exposed to impact type loads depending on their usage area. High strain rate material characterization of metallic materials is very crucial to properly prepare finite element models to be used in impact loading situations. Johnson-Cook material model is a suitable material model to represent the behaviour of metallic materials at high strain rates. In the present thesis study, parameters of the Johnson-Cook material model for Al 7075-T651 are determined utilizing the tensile test data in quasi-static loading condition and impact test data for impact loading condition. High strain rate material characterization of the metallic material is performed by the modified Taylor impact test and velocity interferometry. Modified Taylor impact test system and how the free surface velocity measurement by the velocity interferometry-VISAR is utilized for the determination of the strain rate constant of the Johnson-Cook material model are described in detail. Experimentally

determined material constants are verified by simulating the modified Taylor impact test in Autodyn and comparing the experimentally and numerically determined free surface velocities.

Keywords: Material Characterization, High Strain Rate, Velocity Interferometry, VISAR, Johnson-Cook Material Model, Modified Taylor Impact Test

ÖZ

TERS TAYLOR ÇARPMA TESTİ VE HIZ İNTERFEROMETRİSİ KULLANARAK YÜKSEK GERİNİM HIZLARINDAKİ MALZEME KARAKTERİZASYONU

Kesemen, Latif

Yüksek Lisans, Havacılık ve Uzay Mühendisliği Bölümü

Tez Yöneticisi : Prof. Dr. Altan Kayran

Eylül 2016, 98 sayfa

Havacılık ve uzay yapılarında kullanılan metalik malzemeler kullanım alanlarına göre çarpma yüklerine maruz kalmaktadır. Metalik malzemelerin yüksek gerinim hızlarında malzeme karakterizasyonu, çarpma yükü koşullarının sonlu eleman modellerinin düzgün bir şekilde hazırlanabilmesi için oldukça önemlidir. Johnson-Cook malzeme modeli metalik malzemelerin **yüksek** gerinim hızlarındaki davranışlarını göstermede kullanılan uygun bir malzeme modelidir. Bu çalışmada, yarı durağan koşullardaki çekme testi verileri ile çarpma yükü altındaki çarpma test verileri kullanılarak Al 7075-651 malzemesinin Johnson-Cook malzeme modeli parametreleri belirlenmektedir. Metalik malzemelerin yüksek gerinim hızlarındaki malzeme karakterizasyonu ters Taylor çarpma testi ile hız interferometrisi yardımıyla ile yapılmaktadır. Ters Taylor çarpma testi sistemi ve Johnson-Cook malzeme modelindeki gerinim hızı parametresinin belirlenmesinde kullanılan hız interferometrisi-VISAR ile serbest yüzeydeki hız ölçümünün nasıl yapılacağı detaylı olarak açıklanmaktadır. Testlerle

elde edilen malzeme parametreleri Autodyn'da yapılan ters Taylor testleri ile ve testlerde ve simülasyonlarda elde edilen serbest yüzey hızlarının karşılaştırmaları ile doğrulanmaktadır.

Anahtar Kelimeler: Malzeme Karakterizasyonu, Yüksek Gerinim Hızı, Hız İnterferometrisi, VISAR, Johnson-Cook Malzeme Modeli, Ters Taylor Çarpma Testi

To My Family

ACKNOWLEDGMENTS

The author wishes to express his deepest gratitude to his supervisor Prof. Dr. Altan Kayran and Dr. Hüseyin Emrah Konokman for their guidance, advice, criticism, encouragements and insight throughout the research.

The author would also like to thank Veysel Koca for his contribution during the experiments.

This study was supported by The Scientific and Technological Research Council of Turkey - Defense Industries Research and Development Institute (TÜBİTAK - SAGE).

TABLE OF CONTENTS

LIST OF TABLES

TABLES

LIST OF FIGURES

FIGURES

LIST OF SYMBOLS

A	Yield strength for Johnson-Cook strength model
A	Area
A	Length of reduced section in tensile test
a	Acceleration
B	Strain hardening coefficient for Johnson-Cook strength model
C	Strain rate coefficient for Johnson-Cook strength model
c	Speed of light
c_e	Elastic wave speed
c_L	Elastic wave speed
c_p	Plastic wave speed
c_0	Elastic wave speed
D	Diameter
E	Young's modulus
F	Force
F	Fringe number
f_0	Emitted light frequency
f_b	Beat frequency
f_d	Doppler shift frequency
G	Shear modulus

G	Gauge length in tensile test
h	Deformed length in Taylor test
J	Invariant
J'	Deviatoric invariant
K_f	Fringe constant
L	Length
m	Mass
m	Temperature exponent for Johnson-Cook strength model
m	Total fringe number
n	Strain hardening exponent for Johnson-Cook strength model
n_D	Index of refraction
N	Number of wave period
p	Pressure
P	Period of cycle
R	Radius
S	Deviator stress
t	Time
T	Plastic Modulus
T	Temperature
T	Torque
T_{ref}	Reference temperature
T_{melt}	Melting temperature

T_{room}	Room temperature
T^*	Homologous temperature
T_0	Temperature where internal energy is zero
U	Velocity
u	Velocity
v	Velocity
ν	Frequency of laser light
x	Undeformed length in Taylor test
Y	Yield stress

Greek Symbols

δ	Index refraction correction factor
ε	Strain
ε_e	Elastic strain
ε_e	Plastic strain
$\dot{\varepsilon}$	Strain rate
Δu_p	Particle velocity
Δu_{fs}	Free surface velocity
λ	Lame constant
λ	Wavelength
σ	Stress
σ_{max}	Maximum stress

σ_{min}	Minimum stress
$\sigma_{principal}$	Principal stress
σ_y	Yield stress
μ_σ	Lode parameter
ρ	Density
τ	Shear stress
τ	Delay time
τ_{max}	Maximum shear stress
τ_y	Yield stress in shear

CHAPTER 1

INTRODUCTION

Impact of materials including high deformations and very fast interactions is very complex phenomenon. Dynamic impact type problems usually cannot be solved analytically. Such problems are generally handled by numerical methods utilizing hydrocodes. Hydrocode is a computer tool to model the media in dynamic conditions. Especially, time-dependent and non-linear problems are commonly solved by using the hydrocodes [8].

Hydrocodes mainly use two significant methods for the solution of high velocity impact problems; Lagrangian method and Eulerian method. In the Lagrangian method, the body is defined by the cells. These cells are connected to each other and they deform and move by the forces and in accordance with the constitutive relations. Lagrangian description is applied to the solid materials mostly. In other words, it is appropriate for materials exposed to the comparatively low strain rates. On the other hand, for the problems at high strain rates (higher than 10^5 s^{-1}) like fluids, Eulerian approach is more convenient. In this technique, cells are fixed but amount of the material in each cell is changed by material flow from one mesh to another. This flow occurs due to calculations containing mass, momentum and energy of the material in any cell and the interactions of this cell with the others. In Figure 1, an example of Lagrangian and Eulerian descriptions of an impact phenomenon is represented [8].

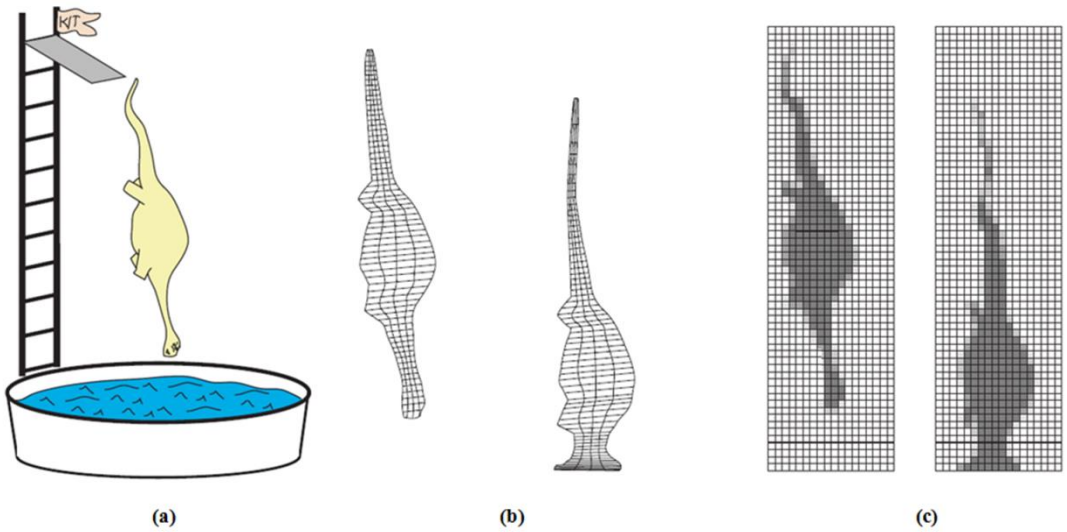

Figure 1 (a) Descriptions of Dinosaur Diving in Illustration (b) Lagrangian (c) Eulerian [8]

Autodyn [1] is one of the most commonly used commercial hydrocodes for dynamic problems. Autodyn has a material library containing many materials with certain properties necessary for dynamic calculations which are related to each other by conservation equations, constitutive equations, equations of state etc. The deformations or movements are computed by using relevant equations and material models. Strength model is one of the most important tools to describe the material response to the dynamic loading in hydrocodes. For example, Johnson-Cook model, which is one of the most common strength models, needs certain parameters to define the deformation of the materials.

Although Autodyn material library includes parameters of strength models for various materials, parameters of many materials such as Aluminum 7075-T651 investigated in this study should be defined by the user. These properties are found by experimental techniques. Characteristics of materials in dynamic conditions can be determined by several test methods such as drop weight test, Split Hopkinson test, Taylor anvil test, flyer plate test etc. Figure 2 shows the strain rate regimes and typical testing methods to characterize the material behavior.

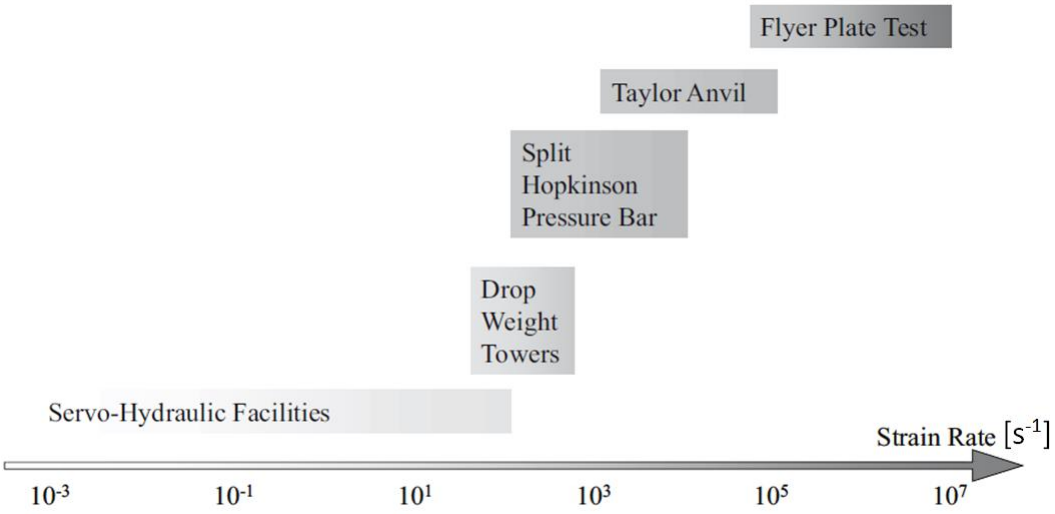

Figure 2 Strain Rate Regimes and Typical Testing Methods to Characterize the Material Behavior [17]

Strain rates in the range of $10^1 – 10^3$ s^{-1} can usually be achieved by the drop impact tests. Drop impact test system also named as drop impact tower is shown in Figure 3. This device transmits a certain amount of energy into a specimen fixed on a support and the rest of the energy is returned to the tup in rebound of the crosshead. In drop tests, a body of known weight, which is released from a certain height, impacts the specimen. The system also includes a velocimetry to measure the impact velocity and a load transducer to measure the contact force. By using the specimen initial position and the impact velocity as initial condition, the velocity of the crosshead and displacement can be determined as a function of time. Also, the amount of the transferred energy between crosshead and specimen is found [25].

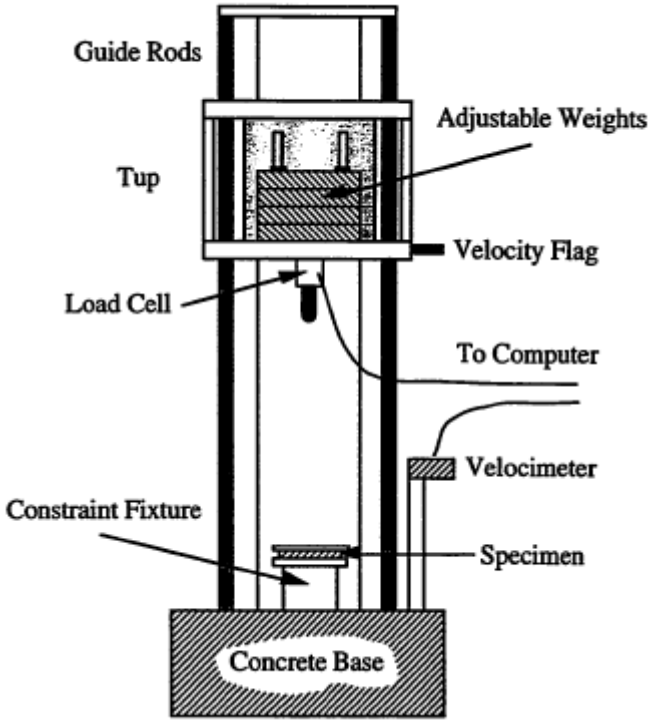

Figure 3 Drop Weight Test Technique [42]

Higher strain rates up to 10^4 s^{-1} can be achieved by the Split Hopkinson test. Figure 5 shows the Split Hopkinson test system. A short and cylindrical specimen is located between two bars which are the incident bar and the transmitted bar. Then, a striker bar is impacted to the incident bar and the sample is exposed to compressive loading. Due to impact, stress wave is generated and it propagates along the bars and the sample. By using strain gages on the incident and the transmitted bars, behavior of the sample can determined. Sample material type affects the wave characteristics thereby allowing one to characterize the material at high strain rate [37].

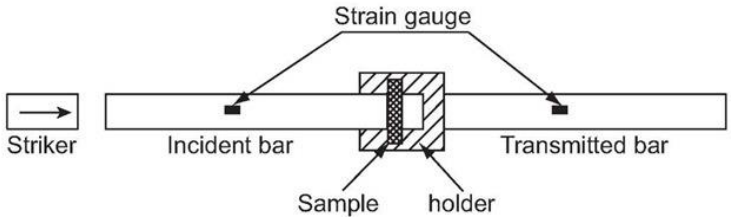

Figure 4 Split Hopkinson Test Technique [20]

Split Hopkinson test technique is also limited by the strain rate based on the material properties of the bars and some other effects. Higher strain rates can be obtained by different methods. Taylor anvil (Taylor impact) and Modified Taylor impact are two commonly used techniques to achieve strain rates up to 10^5 s^{-1}.

1.1. Taylor Impact Test

Geoffrey Taylor [47] offered the Taylor impact test to determine the dynamic yield stress of materials. To achieve this, a cylindrical specimen is impacted to a flat rigid (steel) target as shown in Figure 5. During Taylor impact, elastic and plastic wave propagation affects the plastic deformation of the material [48]. Initially, the impacted specimen has a length of L and velocity of U. At the impact point, elastic and plastic waves start to propagate towards end of the projectile. Since elastic wave is faster than the plastic wave, it reflects from the rear surface and interacts with the plastic wave. The deformation on the body continues during the plastic wave propagation until stress reduces to zero [34].

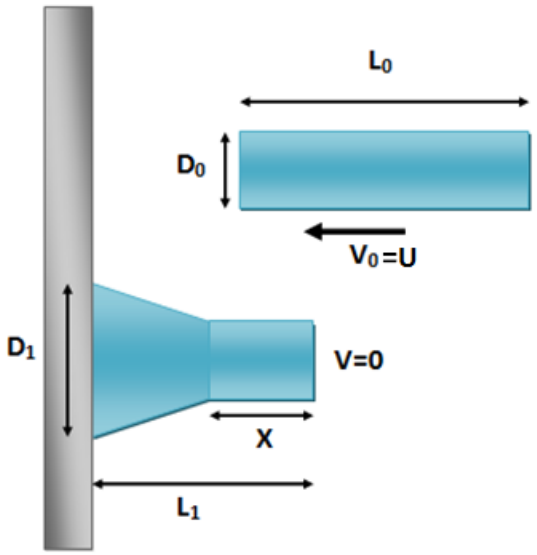

Figure 5 Taylor Impact Test (Initial and final view of the cylindrical specimen)

Taylor impact test is a technique commonly used in the studies about determining the material characteristics under dynamic loadings. Konokman [29] conducted Taylor impact tests and developed a 2-D Lagrangian hydrocode, and compared the test results with the computational ones. In his study, steel specimens at a certain length and diameter are prepared, and impacted to a rigid target with different velocities. Figure 6 shows the deformed shaped of the specimens after impact. Figure 7 shows the deformed shape of the specimen which is obtained by the 2D Lagrangian hydrocode developed.

Figure 6 Taylor Impact Test Results [29]

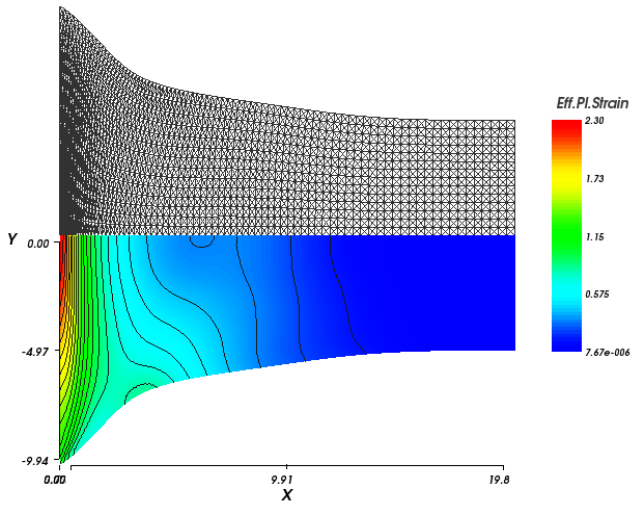

Figure 7 Taylor Impact Analysis Results [29]

Konokman's study includes the verification of a characterized material. In other words, parameters of the Johnson-Cook material model of the specimen material used in these experiments were already known previously. By using dynamic strength parameters of the materials, the analyses are performed to be compared with the experimental results and to verify the hydrocode developed in this study. On the other hand, Yavuz [52] used Taylor impact test technique to define the material behavior in the dynamic conditions. Yavuz also prepared specimens and impacted them to a rigid body. Figure 8 shows the deformed shapes of the specimens after impact. In Yavuz's study, material parameters of the specimens were not known before the tests unlike Konokman's study. After conducting several tests, Johnson-Cook strength model parameters of the materials were obtained by the combination of the Neural Network Model and Autodyn simulations. Neural network model is established for utilizing experimental and analysis results. Figure 9 shows the comparison of the final shapes of the test specimen obtained by the test and Autodyn simulations.

Figure 8 Taylor Impact Test Results [52]

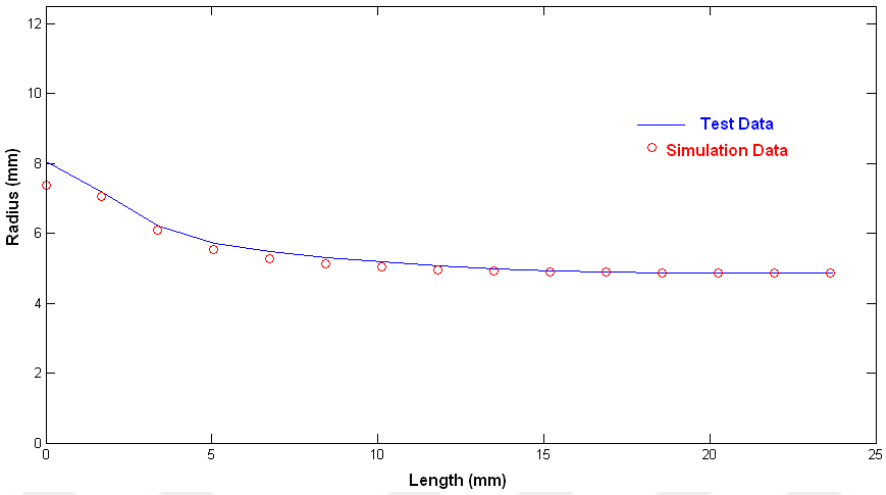

Figure 9 Taylor Impact Analysis Results [52]

The method proposed by Yavuz [43] has some drawbacks since the results are valid for the tests conducted in similar conditions with the previous tests. To obtain more realistic data, number of tests should be increased, and many different cases should be included. For example, the method gives a result for the temperature parameter of Johnson-Cook (*m*) although all the tests are conducted at the same temperature. Temperature parameter cannot be obtained by Taylor tests conducted in constant temperature. It can be concluded that the output of the model is unphysical and it is valid around the conditions which test were conducted.

1.2. Modified Taylor Impact Test

Modified Taylor impact test offered by Rohr et al. [38] is in a way just the opposite of the standard Taylor impact test [48]. In the modified Taylor impact test, instead of the specimen impacting the wall, the wall impacts the specimen. For this purpose, a thin rod is used as the sample, and a relatively larger mass is used as the projectile, as shown in Figure 10. In the modified Taylor impact test [38], a hardened steel projectile with

a 40 mm diameter and a 60 mm length is accelerated to a 35NiCrMoV109 steel sample having 6 mm diameter and 60 mm length.

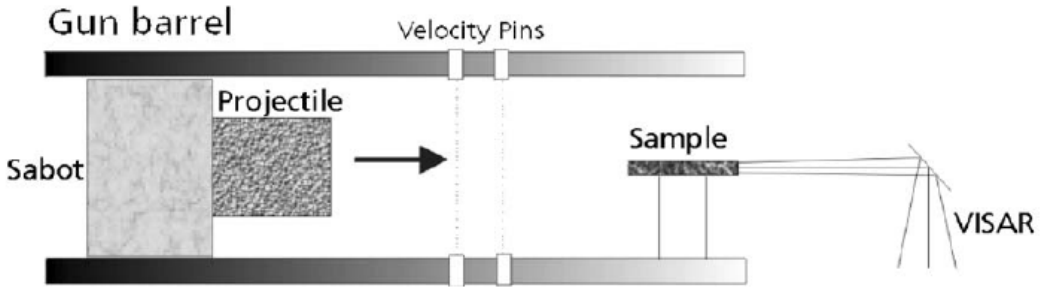

Figure 10 Experimental Setup Representation of the Modified Taylor Impact Test [38]

In order to get reasonable results from the Modified Taylor impact test, certain conditions have to be satisfied. One of them is that the projectile should not deform plastically. To avoid plastic deformation of the projectile, it was selected as steel having 750 HV10 hardness. Another condition is that the specimen length should be relatively longer than its diameter to provide 1-D wave propagation. Therefore, the length of the sample is selected 10 times larger than the diameter [38].

Modified Taylor impact test is developed and integrated to the VISAR measurement technique. VISAR measures the free surface velocity of the specimen during the impact. By using the free surface velocity profile, yield stress, strain, and strain rate are obtained. Also, the results are verified by the numerical simulations which are conducted by the parameters obtained from the experiments [38]. Figure 14 shows the free surface velocity of the sample for different impact velocities.

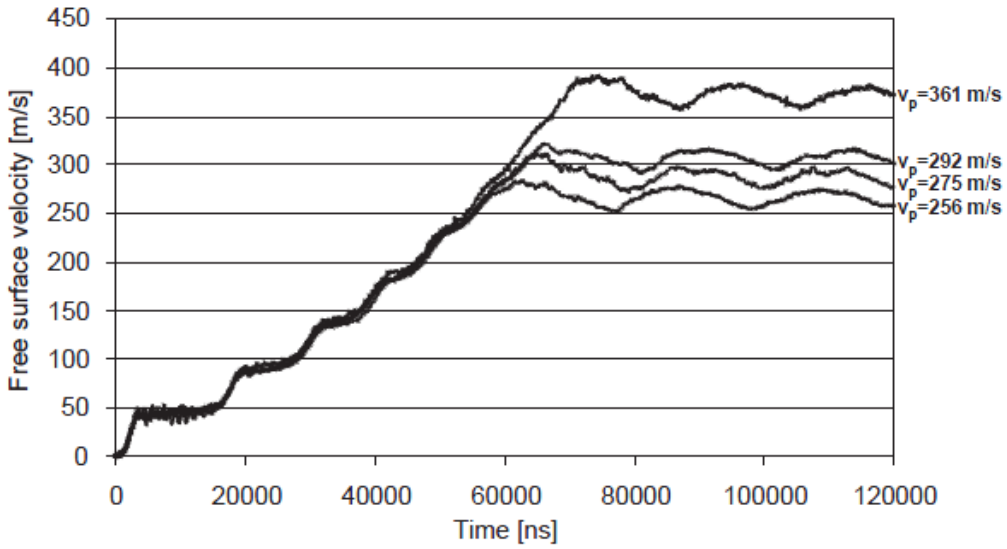

Figure 11 Free Surface Velocity Profile of the Sample [38]

Modified Taylor impact test was also used in various studies. Rohr et al. continued to material characterization by using modified Taylor impact tests. In a study [39], they obtained Johnson-Cook parameters for high strength steel and in another study [40], they obtained the same parameters for a tungsten alloy. Furthermore, Ferranti [10] used this technique to characterize epoxy-cast Al+Fe2O3 material in a PhD's thesis. Forde et al [12] also studied on modified Taylor impact test. Two techniques they used to for obtaining data from the experiments; VISAR and high speed photography. The high speed camera has a capability up to $20x10^6$ frames per second. And, the dynamic material model is obtained for the copper in this study.

1.3. Outline of the Thesis

In this thesis, the material behavior at high strain rates is studied by the modified Taylor impact test and velocity interferometry. Material behavior at high strain rate involves obtaining the stress-strain relation in dynamic conditions. In order to study the impact phenomenon, some basic definitions and theories should be explained first. Therefore, initially, plasticity theory is reviewed in CHAPTER 2. Impact event is described and the relation between the wave theory and the plasticity theory is

explained. Material models which govern the change of material behavior in dynamic conditions are also reviewed in CHAPTER 2.

Material models are achieved experimentally by measurement systems like Split Hopkinson bar technique, photonic Doppler velocimetry and velocity interferometer system for any reflector (VISAR). These systems are explained together with their advantages and limitations in CHAPTER 3.

Experimental tools for high strain rate material characterization are reviewed in CHAPTER 4. Specifically, VISAR, data acquisition system and gas gun systems used in the experimentation are reviewed in CHAPTER 4. Firstly, the sub-parts of VISAR, necessary adjustments for this measurement system and working principal are explained. Although the system makes the measurements during the test, it does not have a memory to record them. For this purpose, an oscilloscope is used as a data acquisition system connected to VISAR to get and use the results in a software platform. VISAR and oscilloscope are integrated in a test area to make the relevant measurements. This area is inside of a cabin mounted to the outlet side of a gas gun. Since such tests are performed by high speed metallic materials and they can be dangerous for any system located closely, some precautions and shielding are applied to protest the very expensive and the weak measurement system. All these integration and setup studies are explained CHAPTER 4. Properties and dimensions of the specimens used in the tensile test and modified Taylor impact test, the test results and unprocessed test data are also presented in CHAPTER 4.

Tensile test is a technique to obtain stress-strain curve of a material in quasi-static conditions. Modified Taylor impact test is commonly used to obtain free surface velocity of a material during the impact phenomenon. The results of both test systems should be processed to determine the Johnson-Cook constitutive parameters. The calculations performed on the test output to determine the parameters of the Johnson-Cook model are given in CHAPTER 5. Specifically, *A, B, C* and *n* parameters of Johnson-Cook strength model are determined. Moreover, the comparison of the experimental results with the Autodyn simulation is also performed. By using the

calculated parameters of the Johnson-Cook strength model, the modified Taylor test is modeled in Autodyn and free surface velocity is also determined by the simulation for the same conditions as the Modified Taylor impact test. Comparison of the free surface velocity profiles are presented in this part.

In this study, Al 7075-T651 material behavior in dynamic condition is investigated. By using the modified Taylor impact test and velocity interferometry (VISAR), Johnson-Cook parameters were obtained for this material. The Autodyn simulation was run by using the aluminum material in which the obtained parameters were used for the strength model. The simulations gave close but not sufficient results compared with the test data. The model was also compared by the results from literature. The simulation was repeated with two different Johnson-Cook model parameters for Al 7075-T651 taken from different studies. The simulation results obtained by this study and literature are close but this comparison also showed that the system should be improved. All of these conclusions are given in CHAPTER 6. Moreover, the future works are explained briefly. Different studies, which can be conducted by using this system in further studies, are mentioned in this part.

CHAPTER 2

THEORY

2.1. Plasticity Theory

2.1.1. Introduction

Materials have three kind of deformation regimes which are elastic, plastic and viscoelastic. Elastic deformation is reversible and time-independent, viscoelastic deformation is reversible and time-dependent, plastic deformation is irreversible and permanent. Materials studied in this thesis are exposed to elastic and plastic deformations mostly. Materials are also classified as brittle and ductile material. Brittle materials exhibit elastic deformation until failure, whereas ductile materials fail after being subjected to plastic deformation [26].

Plasticity theory deals with ductile materials since they undergo plastic deformation. The stress-strain and load-deflection relationships are very critical in plasticity theory. Plasticity theory uses the experimental observations and the mathematical representations, while explaining the relationships between stress and strain or load-deflection. Figure 15 shows the stress-strain curve of mild steel under uniaxial loading. The important points on the curve are marked and they are explained in Table 1 [26].

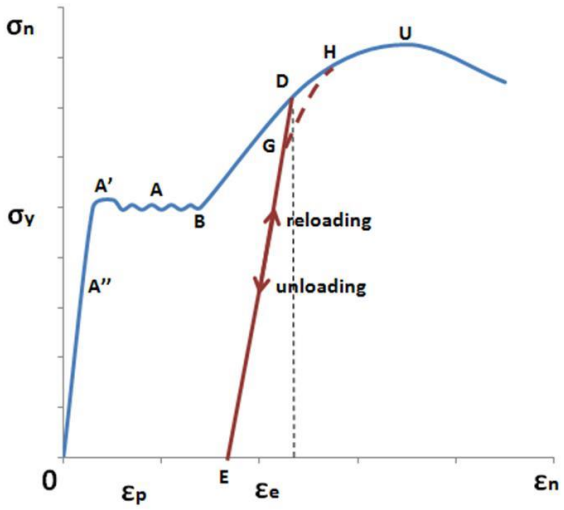

Figure 12 Stress-Strain Curve of Mild Steel under Uniaxial Loading [26]

Table 1 Explanation of Material Behavior in Figure 12

A''	Proportional limit
OA''	Represent by Hooke's law
A'	Upper yield point
AB	Perfectly plastic behavior
A	Elastic limit or yield stress
BU	Work hardening or material hardening
ABU	Plastically deformed
DE	Unloading
EGH	Reloading
EG	Described by Hooke's law
G	Subsequent yield point
A	Initial yield point

2.1.1.1. Incompressibility Effect

Bridgman examined the materials under very high hydrostatic pressure (24000 atm), and concluded that for the metallic materials, under high pressures [26]:

- The volume of material does not change permanently,
- The stress-strain curve does not change,
- The ductility increases,
- Yielding is negligible.

As a summary, metallic materials are plastically incompressible and yielding phenomena is not related with the hydrostatic pressure. Therefore, plasticity theory is not interested with the incompressibility effect [26]. In the plastic range, summation of principal values of plastic strain vanishes as shown in Equation (1).

$$\varepsilon_1 + \varepsilon_2 + \varepsilon_3 = 0 \tag{1}$$

2.1.1.2. Bauschinger Effect

Bauschinger effect states that if a specimen is loaded in tension or compression in one direction until yielding, and then the load is applied in the opposite direction, the yield point in the reverse direction will be lower. As seen in Figure 13, first tensile loading is applied to the material. Then, the load is removed, and compressive load is applied to the same material. In Figure 13, it is seen that yield stress of tensile loading is higher than the compression one. Bauschinger effect is observed in polycrystalline metals and single crystals, and in order to model the Bauschinger effect, kinematic hardening model can be used as shown in the right part of Figure 13 [26]. In the kinematic hardening model, if the tensile yield stress is exceeded, the compressive yield stress reduces but the sum of the tensile and compressive yield stress remains constant. In other words, the total elastic range is maintained constant throughout the deformation.

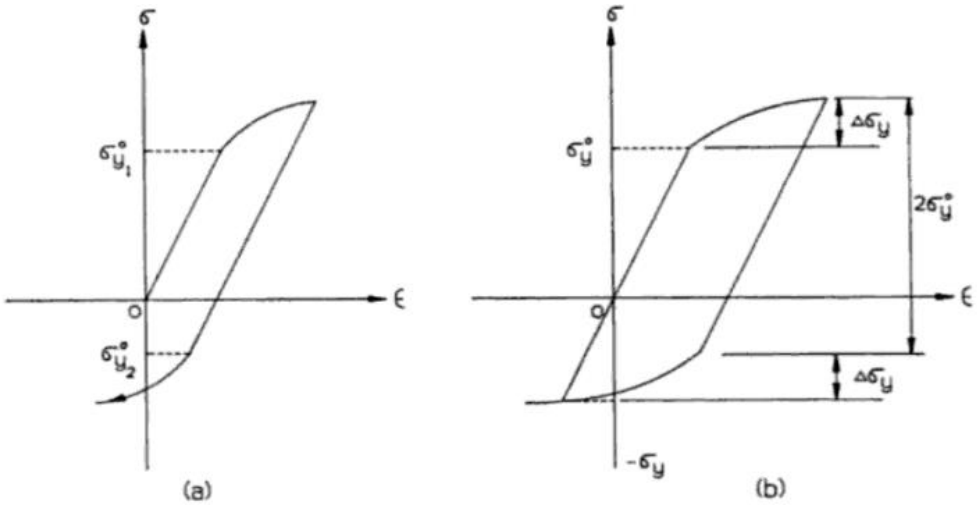

Figure 13 Bauschinger Effect (a) Experimental Result (b) Kinematic Hardening Model [26]

2.1.1.3. Strain Rate Effect

Strain rate effect is one of the most significant effects for the determination of the yield stress in dynamic conditions. It refers to the speed of the change of strain. Strain rate has an effect on the stress-strain relation. The stress-strain curve in the quasi-static loading, for which the strain rate is about $10^{-2} – 10^{-3}$ s^{-1}, is not the same under higher strain rates. Higher strain rates increase the yield stress but decrease the ductility of the metallic materials as shown in Figure 14 [26].

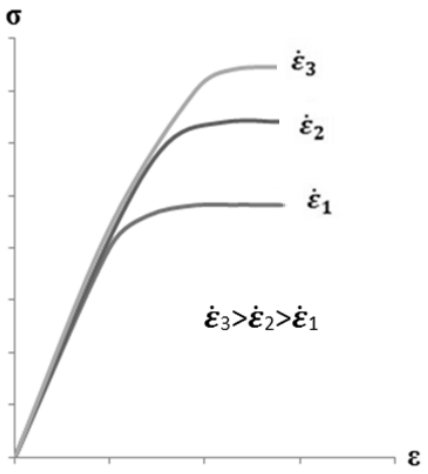

Figure 14 Strain Rate Effect on the Stress Strain Behaviour [26]

2.1.1.4. Temperature Effect

Temperature has an opposite effect on the metallic material behavior compared to the strain rate effect. Temperature increase causes material to be more ductile. Increase of temperature also decreases the yield point as shown in Figure 15 [26].

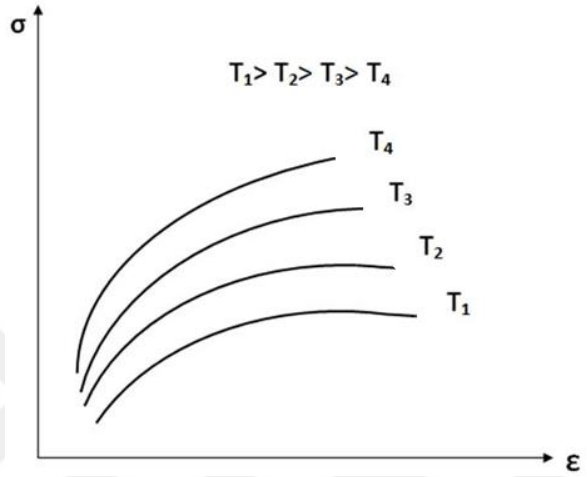

Figure 15 Temperature Effect on the Stress Strain Behavior [26]

2.1.2. Yield Criteria

Yield stress (σ_y) is used to define the yield point of a material which divides elastic and plastic regions into two parts for the one dimensional case. In three dimensions, yield surface separates the elastic and the plastic domains by a continuous surface, and it can be considered as a boundary between the two domains [26]. In the plastic domain, the materials deform permanently and there are several criteria explaining this phenomenon. This section gives the basic definitions and yield criteria used to define the yield stress.

Stress tensor (σ), which is used to represent the stress state at any point of a material, is a second order matrix. Moreover, it is a symmetric tensor, and it has six independent components.

$$\sigma_{ij} = \begin{bmatrix} \sigma_{xx} & \sigma_{xy} & \sigma_{xz} \\ \sigma_{yx} & \sigma_{yy} & \sigma_{yz} \\ \sigma_{zx} & \sigma_{zy} & \sigma_{zz} \end{bmatrix} \quad (2)$$

In Equation (2), σ_{xx}, σ_{yy}, σ_{zz}, σ_{xy}, σ_{yz}, σ_{xz} are six independent variables since stress tensor is symmetric and $\sigma_{xx,}$ σ_{yy} and σ_{zz} are the normal stresses. If the state of stress at a material point is such that all the shear stress components are zero, then normal stresses are named as principal stresses. Principal stresses can be calculated by using as,

$$\left|\sigma_{ij} - \sigma\delta_{ij}\right| = 0 \quad (3)$$

which can be also written as given in Equation (9).

$$\begin{vmatrix} \sigma_{xx} - \sigma & \sigma_{xy} & \sigma_{xz} \\ \sigma_{yx} & \sigma_{yy} - \sigma & \sigma_{yz} \\ \sigma_{zx} & \sigma_{zy} & \sigma_{zz} - \sigma \end{vmatrix} = 0 \quad (4)$$

Expanding Equation (4),

$$\sigma^3 - J_1\sigma^2 + J_2\sigma - J_3 = 0 \quad (5)$$

where J_1, J_2 and J_3 are the coefficients of the eigenvalues of the stress tensor. These coefficients are called as first, second and third invariants. The invariants are constant and do not depend on the orientation of the coordinate system. J_1 is the first invariant given by Equation (11).

$$J_1 = \sigma_{xx} + \sigma_{yy} + \sigma_{zz} \quad (6)$$

In addition to the first invariant, there are two other stress invariants. J_2 is the second invariant and given by;

$$J_2 = \sigma_{xx}\sigma_{yy} + \sigma_{yy}\sigma_{zz} + \sigma_{xx}\sigma_{zz} - {\sigma_{xy}}^2 - {\sigma_{xz}}^2 - {\sigma_{yz}}^2 \quad (7)$$

and J_3 is the third invariant given by Equation (8).

$$J_3 = \begin{vmatrix} \sigma_{xx} & \sigma_{xy} & \sigma_{xz} \\ \sigma_{yx} & \sigma_{yy} & \sigma_{yz} \\ \sigma_{zx} & \sigma_{zy} & \sigma_{zz} \end{vmatrix} \quad (8)$$

The solution of the Equation (5) gives the principal stresses σ_1, σ_2 and σ_3 which can be represented by the diagonal matrix given by Equation (9).

$$\sigma_{principal} = \begin{vmatrix} \sigma_1 & 0 & 0 \\ 0 & \sigma_2 & 0 \\ 0 & 0 & \sigma_3 \end{vmatrix} \quad (9)$$

Figure 16 shows the state of stress at a material point and the principal stress planes.

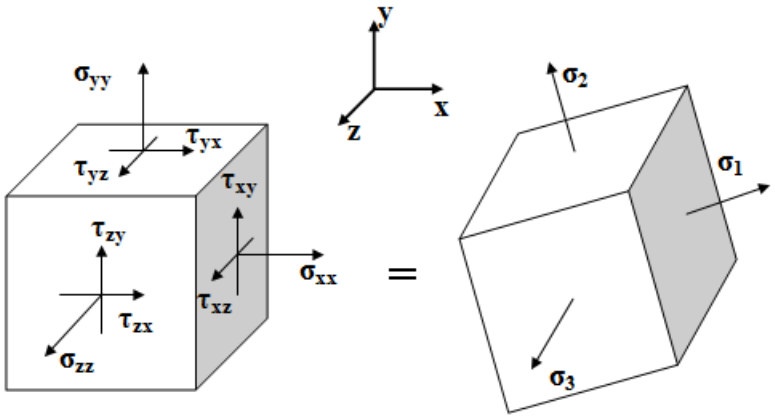

Figure 16 Stress State at a Material Point and the Principal Stress Planes

Plasticity theory uses the principal stresses to decompose the stress tensor into two parts which are the hydrostatic stress (pressure, $p\delta_{ij}$), and the deviatoric stress (S_{ij}), as shown in Equation (10).

$$\sigma_{ij} = p\delta_{ij} + S_{ij} \quad (10)$$

Since the hydrostatic part does not contribute to plastic deformation as mentioned in the section 2.1.1.1, plasticity theory is interested only on the deviatoric part of the stress.

Hydrostatic stress term can be defined by the principal stresses as given in Equation (11).

$$p = \frac{1}{3}\left(\sigma_{xx} + \sigma_{yy} + \sigma_{zz}\right) = \frac{1}{3}(\sigma_1 + \sigma_2 + \sigma_3) \tag{11}$$

Deviatoric stress is then defined by Equation (12).

$$S_{ij} = \sigma_{ij} - p\delta_{ij} \tag{12}$$

Deviatoric stress S_{ij} can be also defined by principal stresses in terms of the principal stresses of the stress tensor. Deviatoric principal stresses are given in Equations (13), (14) and (15).

$$S_1 = \frac{2\sigma_1 - \sigma_2 - \sigma_3}{3} \tag{13}$$

$$S_2 = \frac{2\sigma_2 - \sigma_1 - \sigma_3}{3} \tag{14}$$

$$S_3 = \frac{2\sigma_3 - \sigma_1 - \sigma_2}{3} \tag{15}$$

Since there is no hydrostatic stress in the deviatoric part, sum of principal deviatoric stresses should be zero, as shown in Equation (16);

$$S_1 + S_2 + S_3 = 0 \tag{16}$$

Equation (16) is also the new invariant J_1', defined in terms of principal deviatoric stress. And the other deviatoric invariants J_2' and J_3' are defined by Equation (17) and Equation (18), respectively.

$$J_2' = \frac{1}{3}(J_1^2 - 3J_2) \tag{17}$$

$$J_3' = 27(2J_1^3 - 9J_1J_2 - 27J_3) \tag{18}$$

It should be noted that to define the deformation limit of the materials yield criterion is needed. There are two most commonly used yield criteria for the metallic materials known as von-Mises and Tresca [26].

von Mises criterion, also called distortion energy criterion, states that plastic deformation in a material occurs when the distortional strain energy exceeds the energy limit for yielding in the uniaxial tension test. The yield stress is derived by the distortional strain energy as given in Equation (19).

$$\sigma_y = \frac{1}{\sqrt{2}}[(\sigma_1 - \sigma_2)^2 + (\sigma_2 - \sigma_3)^2 + (\sigma_3 - \sigma_1)^2]^{1/2} \quad (19)$$

If pure torsion load is applied to the material, then σ_2 is zero and σ_1 and $-\sigma_3$ are equal to yield stress in pure shear test τ_y as shown in Equation (20)

$$\sigma_1 = -\sigma_3 = \tau_y \quad (20)$$

By using Equation (19) and Equation (20), Equation (21) is obtained as given below.

$$\tau_y = \frac{\sigma_y}{\sqrt{3}} \quad (21)$$

Tresca criterion briefly states that the plastic deformation occurs in a material when the maximum shear stress reaches the shear stress when the yielding occurs in the uniaxial tensile test. From Mohr's circle, it is known that half of the difference of the principal stresses gives the maximum shear stress. The maximum shear stress can be calculated by using the difference between the maximum and minimum principal stresses, as shown in Equation (22).

$$\frac{1}{2}(\sigma_{max} - \sigma_{min}) = \tau_{max} \quad (22)$$

In a uniaxial test, when the axial stress σ_1 reaches the yield stress σ_y, while the other normal stresses are zero, maximum shear stress is given by Equation (23).

$$\frac{\sigma_y}{2} = \tau_{\max} \tag{23}$$

In three dimensions, yield stress can be written in terms of principal stress by Equation (24);

$$\sigma_y = max[|\sigma_1 - \sigma_2|, |\sigma_1 - \sigma_3|, |\sigma_2 - \sigma_3|] \tag{24}$$

von Mises and Tresca are two criteria offered for the yield stress. There are several studies conducted to compare these criteria [26]. Lode [31] performed experiments to find the best yield criterion that gives outcomes closer to the experimental results. For this purpose, thin-walled tubes of various materials were used in uniaxial tension and internal pressure loadings together. Before beginning to the tests, a parameter μ_σ, given in Equation (25), was defined in terms of the principal stresses as follows;

$$\mu_\sigma = \frac{2\sigma_2 - \sigma_1 - \sigma_3}{\sigma_1 - \sigma_3} \tag{25}$$

where $\sigma_1 > \sigma_2 > \sigma_3$. Since σ_2 has the middle value between the principal stresses and Tresca yield criterion is defined only by the maximum and minimum principal stresses, Tresca criterion cannot be written in terms of σ_2 or the μ_σ parameter. Tresca yield criterion can be written in terms of σ_1 and σ_3 as in Equation (26).

$$\frac{\sigma_1 - \sigma_3}{\sigma_y} = 1 \tag{26}$$

von Mises criterion depends on all principal stresses and it can be written in terms of σ_1, σ_2 and σ_3. To eliminate σ_2, it is written in terms of μ_σ, σ_1 and σ_3 and the von Mises yield criterion is obtained as shown in Equation (27).

$$\frac{\sigma_1 - \sigma_3}{\sigma_y} = \frac{2}{\sqrt{3 + {\mu_\sigma}^2}} \tag{27}$$

In Lode's study, experiments were conducted to obtain the change of $\frac{\sigma_1 - \sigma_3}{\sigma_y}$ by μ_σ and compare them with the theoretical results. Lode pressurized a thin-walled tube up to *p* and applied a force *F* uniaxially. For this load case, tangential and axial stresses can be written as,

$$\sigma_\theta = \frac{pR}{t} \tag{28}$$

$$\sigma_z = \frac{F}{2\pi Rt} \tag{29}$$

$$\sigma_r \approx 0 \tag{30}$$

where $\sigma_\theta = \sigma_1$, $\sigma_z = \sigma_2$ and $\sigma_r = \sigma_3$=0.

Utilizing Equation (25), (28), (29), (30), μ_σ parameter can be written as,

$$\mu_\sigma = \frac{F - \pi R^2 p}{\pi R^2 p} \tag{31}$$

By controlling the axial force *F* and the internal pressure *p*, μ_σ value was obtained in the range -1 to 1. It should be noted that Tresca yield criterion is not affected by the change in μ_σ because it is independent of μ_σ and $\frac{\sigma_1 - \sigma_3}{\sigma_y}$ is equal to 1 for all value of μ_σ. On the other hand, von Mises yield criterion depends on the μ_σ parameter. As seen in Figure 17, experimental results are mostly located around the von Mises curve, not around the Tresca curve. These experiments proved that von Mises yield criterion is more realistic than Tresca's.

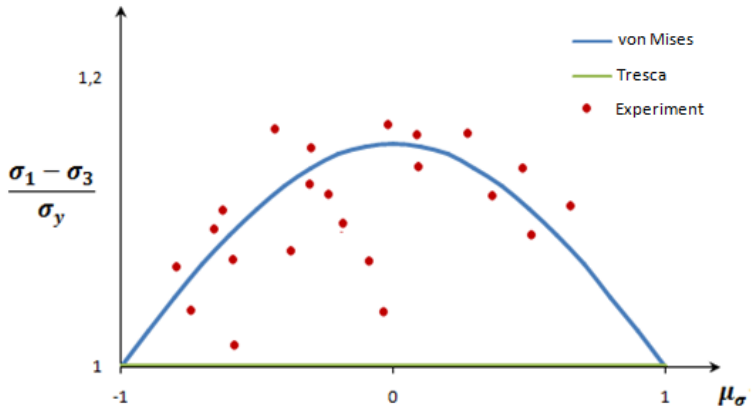

Figure 17 Lode's Comparison of von Mises and Tresca Yield Criteria with the Experiment Results [26]

Taylor and Quiney [20] also used thin-walled tubes of different materials, but applied uniaxial force *F* and torque *T* unlike the Lode's experiments. von Mises and Tresca yield criteria are written in terms of normal stress, shear stress, and yield stress as in Equation (32) and Equation (33), respectively. Normal stress is proportional to axial force *F*, shear stress is proportional to torque *T* and they are independent of each other.

$$\left(\frac{\sigma}{\sigma_y}\right)^2 + 3\left(\frac{\tau}{\sigma_y}\right)^2 = 1 \tag{32}$$

$$\left(\frac{\sigma}{\sigma_y}\right)^2 + 4\left(\frac{\tau}{\sigma_y}\right)^2 = 1 \tag{33}$$

By controlling the axial force *F* and the torque *T*, $\frac{\tau}{\sigma_y}$ versus $\frac{\sigma}{\sigma_y}$ plots were drawn for various materials like copper, mild steel, and aluminum. Figure 18 compares the von Mises and Tresca yield criteria with the experimental results. The yield stress is assumed as the yield point at uniaxial test where both criteria verify this stress at the given point. Again, Figure 18 shows that von Mises yield criterion represents the yielding of annealed copper better compared to the Tresca yield criterion.

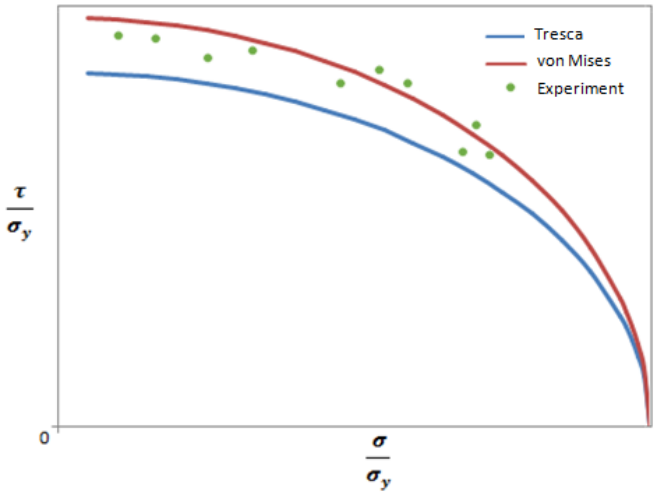

Figure 18 Taylor and Quiney's Comparison of von Mises and Tresca Yield Criteria with the Experiment Results for Annealed Copper [26]

Lianis and Ford [30] used notched specimen of pure aluminum material in the experiments to define the yielding. Lianis and Ford's experiments also support that von Mises theory is more compatible with the experimental results than the Tresca yield criterion. It should also be noted that most of the commercial codes prefer von Mises yield criterion in problems involving plasticity [26].

2.2. Impact Mechanics

Impact mechanics investigates the wave propagation, fracture, penetration aspects of materials subjected to impact loading. Modified Taylor impact test, which is studied in the present thesis, is also the subject of impact mechanics. Understanding the wave propagation mechanism in materials subject to impact loading is very important to characterize the material behavior.

Wave propagation in solid media occurs by elastic waves, plastic waves, shock waves and viscoelastic waves [41]. Elastic wave propagation occurs at loads below the yield point. When the load is increased higher than the yield point, material begins to behave plastically. Plastic waves are slower but cause the plastic deformations on the media. Generally, plastic wave propagation is studied in long rod geometries to neglect the lateral inertia and thermal effects [56].

2.2.1. Elastic Waves

Elastic deformation is the recoverable part of the deformation. In case of elastic deformation, deformed material returns to its original shape. Elastic wave is a mechanical disturbance that propagates through a material causing oscillations of the particles about their equilibrium positions but it does not cause any other change [49].

Elastic theory states that there are two kind of elastic waves; dilatational (longitudinal / compressive), and distortional (transverse) waves for the isotropic solids. Dilatational waves are also called longitudinal wave since they move in the direction of perpendicular to the wave front. Distortional waves are shear waves propagating parallel to the wave front [56].

In 1-D motion, if the striker bar impacts the cylindrical bar below the elastic-plastic boundary, elastic wave is generated along the bar. In Figure 19, the striker bar impacts the long cylindrical bar at a velocity *V* and compressive stress wave that is generated in the bar travels from left to the right. In Figure 19, the infinitesimal section shown is considered to be at the front of the stress wave at time *t* [10].

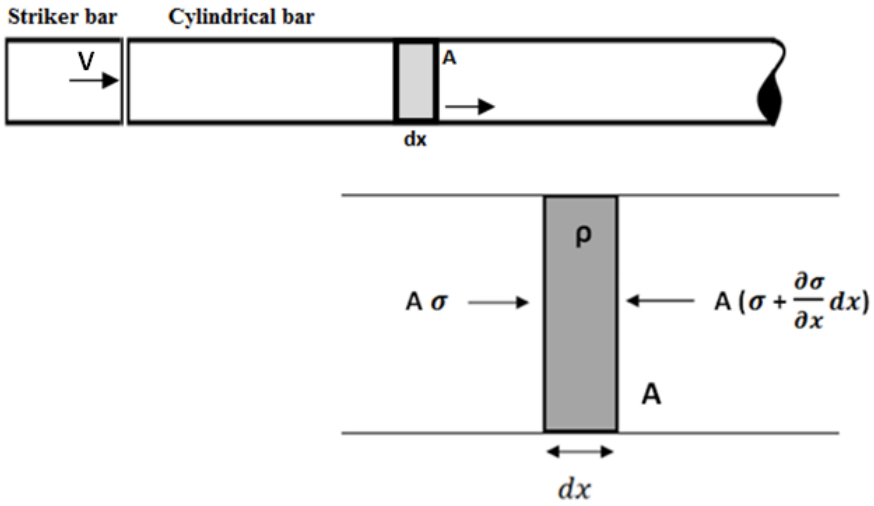

Figure 19 Forces on a Cylindrical Bar in 1-D Wave Motion [10]

Elastic wave velocity for the bounded media can be obtained by using constitutive relations. Firstly, Newton's second law is written as given in Equation (34).

$$F = ma = m\frac{\partial^2 u}{\partial t^2} \tag{34}$$

where u is the particle velocity.

Applying Newton's second law to the section having thickness dx and area A of the cylindrical rod shown in Figure 19, Equation (34) can be written as shown in Equation (35).

$$-\left[A\sigma - A\left(\sigma + \frac{\partial \sigma}{\partial x}dx\right)\right] = A\rho\frac{\partial^2 u}{\partial t^2}dx \tag{35}$$

Hooke's law is given in Equation (36),

$$\frac{\sigma}{\varepsilon} = E \tag{36}$$

where ε is the strain defined as $\partial u/\partial x$. By utilizing the Equation (35), and (36), Equation (37) is obtained.

$$\frac{\partial^2 u}{\partial t^2} = \frac{E}{\rho}\frac{\partial^2 u}{\partial x^2} \tag{37}$$

The general form of the 1-D wave equation is given by Equation (38).

$$\frac{\partial^2 u}{\partial t^2} = c^2\frac{\partial^2 u}{\partial x^2} \tag{38}$$

By using the Equations (37) and (38), elastic wave speed c_0 can be expressed in terms of E and ρ as shown in Equation (39).

$$c_0 = \sqrt{\frac{E}{\rho}} \tag{39}$$

2.2.2. Plastic Waves

The response of material to dynamic loading is determined by the equilibrium equations of motion and constitutive equations of the materials. If the loading applied to the material exceeds the yield point, plastic waves occur in addition to elastic waves. These waves interact between each other in a finite bar during their propagation and the plastic wave effects should be considered also to define the yield stress correctly. Thus, the relation between yield stress and wave speeds in the elastic range can be determined [10].

Elastic wave definition is given in the section 2.2.1. For the plastic wave propagation, a mathematical description of the material behavior is required as a function of strain. Karman and Duwez [24] developed plastic wave propagation theory in 1942. This theory firstly describes that stress is basically a function of strain ($\sigma=\sigma(\varepsilon)$). The theory neglects the three dimensional effects and it is completely uniaxial. For the 1-D uniaxial case and elastic wave propagation, the equation of motion is derived from the Newton's second law described in section 2.2.1. However, this formulation is not valid for the plastic range. Equation (37) can be written to cover both elastic and plastic ranges as shown by,

$$\rho \frac{\partial^2 u}{\partial t^2} = T \frac{\partial^2 u}{\partial x^2} \tag{40}$$

where $T=d\sigma/d\varepsilon$ is equal to elastic modulus below yield point (constant and equal to E) or plastic modulus above yield point. Stress – strain relation is shown in Figure 20 for the elastic and the plastic region.

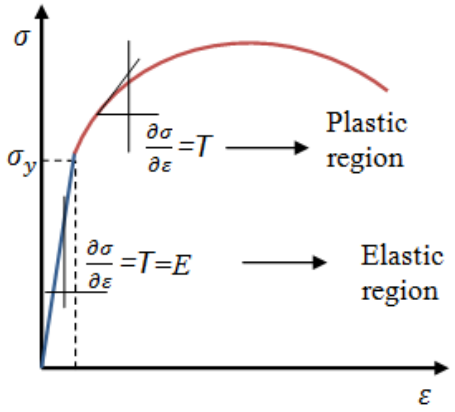

Figure 20 Stress-Strain Curve in Elastic and Plastic Regions

For the semi-infinite bar, boundary condition is defined as follows to determine the wave profile within the material,

$$u = \begin{cases} v_1 t \ at \ x = 0 \\ 0 \ at \ x = -\infty \end{cases} \tag{41}$$

where v_1 is the particle velocity for the semi-infinite bar. Solutions of Equation (40) are found in different regions and they are given by Equations (42), (43) and (44).

$$u = v_1\left(t + \frac{x}{c_1}\right) \ or \ \varepsilon = \frac{\partial u}{\partial x} = \frac{v_1}{c_1} = constant \tag{42}$$

$$\frac{T}{\rho} = \frac{x^2}{t^2} \tag{43}$$

$$\varepsilon = 0 \tag{44}$$

These three equations give the complete solution when combined.

(a) For $|x|<c_1t$, c_1 is the velocity of the plastic wave front and the strain is constant and equal to ε_1,

(b) For $c_1t<|x|<c_0t$, c_0 is the velocity of the elastic wave front, where $x/t = (T(\varepsilon)/\rho_0)^{1/2}$,

(c) For $|x|>c_0t$, $\varepsilon=0$.

If we define $\xi=x/t$, strain versus ξ relation can be graphically as in Figure 21.

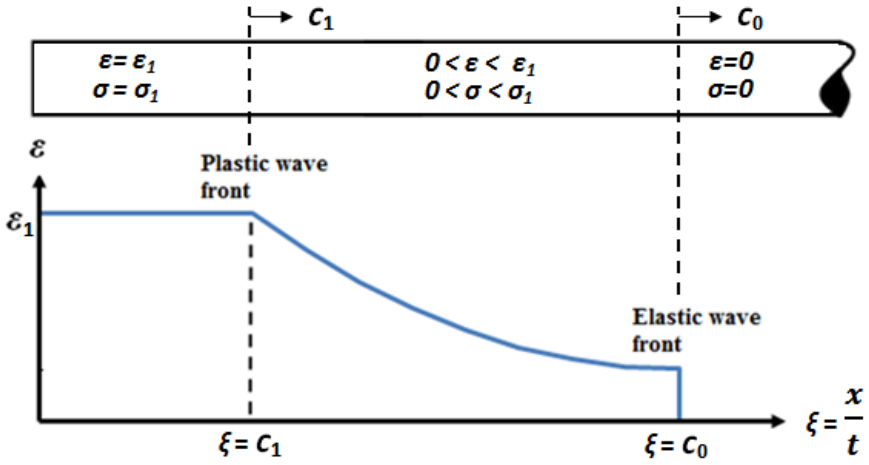

Figure 21 Elastic and Plastic Wave Profiles [24]

As shown in Figure 21, elastic and plastic waves propagate at different velocities. The plastic wave velocity c_1 and the maximum strain ε_1 as a function of impact velocity v_1 must be determined to find the yield stress in elastic range. By assuming $\varepsilon=f(\xi)$ where $\xi=x/t$, the displacement u can be written as Equation (45).

$$u=\int_{-\infty}^{x}\frac{\partial u}{\partial x}dx=\int_{-\infty}^{x}f(\xi)dx=t\int_{-\infty}^{0}f(\xi)d\xi \tag{45}$$

By using Equation (45), Equation (46) is obtained.

$$v_1=\frac{u(0,t)}{t}=\int_{-\infty}^{0}f(\xi)d\xi \tag{46}$$

And by changing the variables, Equation (46) can be written in terms of ε as given in Equation (47).

$$v_1=\int_{0}^{\varepsilon_1}\xi d\xi \tag{47}$$

Next, upon substituting for ξ from Equation (43), Equation (48) can be obtained.

$$v_1 = \int_0^{\varepsilon_1} \left(\frac{T(\varepsilon)}{\rho_0}\right)^{1/2} d\varepsilon \tag{48}$$

If the deformation remains in the elastic limit, $T=E=constant$ and $v_1=\varepsilon_1 c_0$. Then, one can write;

$$v_1 = \varepsilon_1 \left(\frac{E}{\rho_0}\right)^{1/2} \tag{49}$$

$$\sigma_1 = E\varepsilon_1 = \rho_0 v_1 c_0 \tag{50}$$

Equation (50) is used for the calculation of stress in the elastic range for an impact velocity v_1. If stress remains within the elastic limit range, there are two regions; for $|x|<c_0t$, $\sigma=\rho v_1 c_0$ and for $|x|>c_0t$, $\sigma=0$. If the stress exceeds the elastic limit, plastic waves are produced and there are two fronts in this case as shown in Figure 21. At the front of the elastic wave, the stress is $\sigma=0$ zero and it increases to maximum stress $\sigma=\sigma_1$ gradually. Behind the front of the plastic wave, σ has the constant value σ_1 corresponding to the total strain ε_1 [24].

2.2.3. Relationship between the Wave Propagation and Yield Stress

Taylor [48] developed a test system to determine the dynamic yield strength of materials. The experiment is conducted by impacting a cylindrical specimen with length L against a rigid anvil with velocity U. Following the experiment, the final deformed body of the specimen is investigated to determine the yield stress of the material. The simplified system is shown in Figure 22. Upon the impact, elastic wave begins propagating through the rod and comparatively slower plastic wave follows it. The stress that occurs in the deformed region is assumed as constant and equal to yield stress at a unique strain. The elastic wave continues to propagate such that it reflects from the back surface and returns towards the propagating plastic wave. And once again, the elastic wave reflects from the plastic wave and returns towards the back surface of the specimen. In each interaction between the elastic and the plastic wave, the stress decreases and this process continues until the stress becomes zero [24].

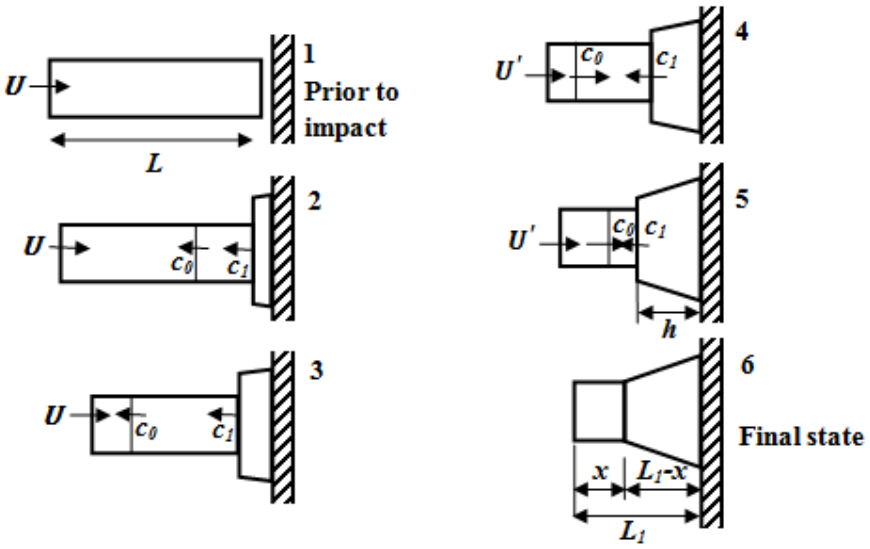

Figure 22 Simplified Deformation Steps of the Cylindrical Specimen in Taylor Impact Test [34]

Wilkins and Guinan [51] offered a correlation between the yield stress and the final length of the projectile by using the elastic-plastic theory. Firstly, they found that the ratio of the final length of the projectile to initial length was constant for each velocity. In their analysis, it was assumed that the projectile decelerates as a rigid body and the plastic deformation occurs at the impact face. Therefore, the change in the specimen length over time is equal to the instantaneous particle velocity U given in Equation (51).

$$\frac{dL}{dt} = -U \tag{51}$$

The force applied by the deceleration of the specimen is equal to the product of the dynamic stress σ_{yd} and the cross-sectional area A. Equation (52) can be written by applying the Newton's second law such that the mass is equal to $\rho_0 LA$ and deceleration of the specimen is equal to dU/dt.

$$\sigma_{yd} A = -\rho_0 LA \frac{dU}{dt} \tag{52}$$

By combining the Equations (51), and (52), the Equation (53) can be obtained.

$$\frac{dL}{L} = \frac{\rho_0 U}{\sigma_{yd}} dU \tag{53}$$

$L = L_0$ is the initial length; $L = L_1$ is the final length.

$U=U$ is the initial velocity; $U=0$ is the final velocity.

By integrating the Equation (53) and by applying the boundary conditions Equation (54) is obtained.

$$\sigma_{yd} = \frac{\rho_0 U^2}{2\ln(L_1/L_0)} \tag{54}$$

Thus, dynamic yield strength of the specimen can be estimated by Equation (54) using density, velocity, and final and initial lengths of the specimen [24].

Modified Taylor test is conducted with velocity interferometry (VISAR) to measure the material response during the impact [39]. The present thesis is on the setup of this test system and material characterization by using it. In this test system, a specimen is held stationary and a rigid anvil accelerated by a gas gun to impact the specimen. Upon impact, VISAR measures the velocity of the back surface of the specimen as given in Figure 23. This measurement shows the elastic wave propagation along the specimen. Back surface of the specimen velocity increases step by step at each reflection of elastic wave from this surface. By using the velocity step value (free surface velocity) and its duration, dynamic strength and the strain rate of the material are determined.

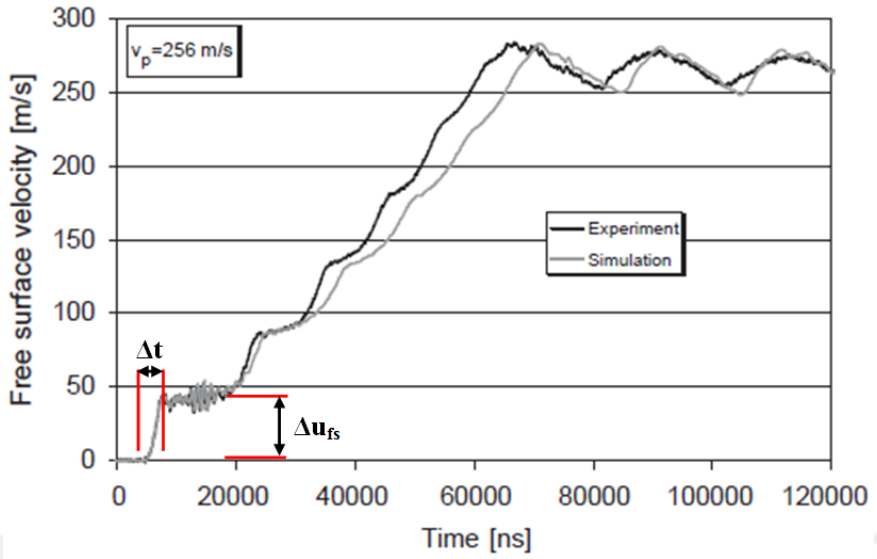

Figure 23 Free Surface Velocity Profile of a Steel Specimen obtained in Modified Taylor Impact Test by VISAR [39]

Figure 24 represents of elastic and plastic wave propagation along a thin rod schematically. The wave behavior is the same with the rods used in the Taylor impact tests explained above. Upon impact, elastic wave travels through the specimen until reflecting from the back surface. During this reflection, the motion of this wave causes the velocity increase measured by the VISAR. VISAR sends a laser beam to the specimen back surface and the reflected beam returns to the VISAR. The returned beam splits and interferences to measure the frequency change of the laser during the motion of the back surface. At acceleration of this surface, VISAR finds the surface velocity by using the frequency and intensity change of the laser.

As mentioned before, wave propagation elastic wave reflects from the back surface and the plastic wave respectively. The elastic wave travel and the stepwise velocity increase that it causes are shown in Figure 24. Plastic wave is also reflected from the impact surface and the elastic wave respectively. During the wave propagation, plastic wave deforms the specimen.

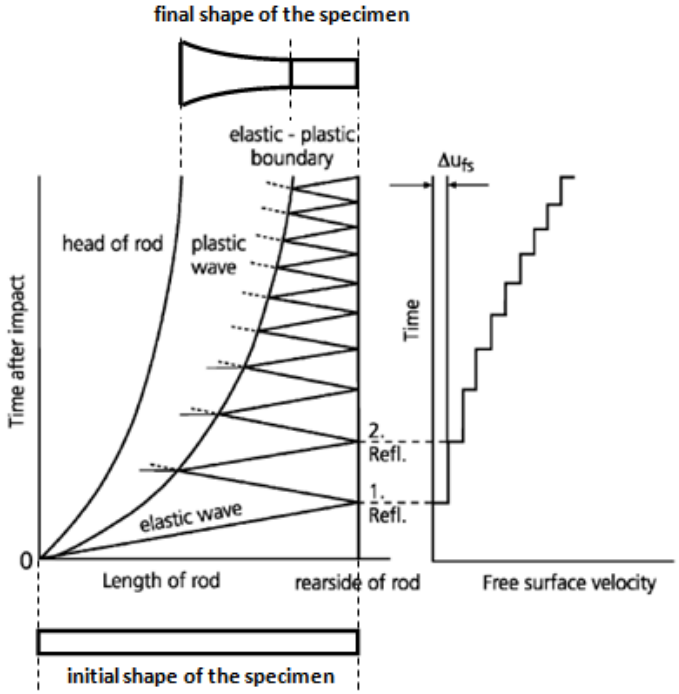

Figure 24 Schematic Representation of Elastic and Plastic Wave Propagation Interaction along a Thin Rod after Impact [39]

To determine the relation between the yield strength and the free surface velocity profile, 1-D wave equation defined in Equation (38) has to be solved for a complete reflection of an elastic wave from the surface. The wave equation for the propagation of an elastic compression wave along a thin rod is given as,

$$\frac{\partial^2 u}{\partial t^2} = {c_L}^2 \frac{\partial^2 u}{\partial x^2} \tag{55}$$

where u is the disturbance in the rod at time t, $c_L(\sqrt{\frac{E}{\rho}})$ is the elastic wave speed at time t=0. The solution of the Equation (55) can be written as a linear combination of waves moving in $+x$ and $-x$ directions as shown in Equation (56).

$$u = f(c_L t - x) + F(c_L t + x) \tag{56}$$

By differentiating $u = F(c_L t + x)$ with respect to x and t respectively, Equation (57) is obtained.

$$\frac{\partial u}{\partial t} = c_L \frac{\partial u}{\partial x} \tag{57}$$

It should be noted that since the rod has the finite length and the wave propagates in one direction only, wave propagation in the positive x-direction is considered only and therefore u is equated to $F(c_L t + x)$. Utilizing Hooke's law in Equation (57) one gets,

$$\sigma = \frac{E}{c_L}\frac{\partial u}{\partial t} = \rho c_L \Delta u_p = \frac{1}{2}\rho c_L \Delta u_{fs} \tag{58}$$

where $\Delta u_p = \partial u/\partial t$ is the particle velocity that occurs due to the stress induced by the compression pulse in the rod as shown in Figure 23. Since the impact velocity is high enough causing the elastic and plastic wave propagation on the bar, the stress σ is equal to the yield stress. The free surface velocity Δu_{fs} is the velocity change at the back surface of the rod. Then, Equation (58) can be written as,

$$\sigma_{yd} = \frac{1}{2}\rho c_L \Delta u_{fs} \tag{59}$$

The strain in this event can be written as,

$$\varepsilon = \frac{\Delta u_p}{c_L} = \frac{\Delta u_{fs}}{2c_L} \tag{60}$$

And the strain rate is obtained as Equation (61).

$$\frac{d\varepsilon}{dt} = \frac{\varepsilon}{\Delta t} \tag{61}$$

2.3. Dynamic Strength Models

Dynamic strength models are used to characterize the mechanical behavior of materials under high loadings and high strain rates. Materials behavior in dynamic conditions can be quite different than in quasi-static conditions. For example, yield point of a material can be higher in high strain rates compared to low strain rates. The

models representing such behavior of materials are called dynamic strength models. Johnson-Cook model, Zerilli-Amstrong model, Mechanical Threshold Stress model, Steinberg and Lund model, Preston, Tonks and Wallace model are some of the most common examples of these models.

2.3.1. Johnson-Cook Model

Johnson-Cook material model is one of the simplest dynamic strength models. Although other models can predict the dynamic behavior of some materials better than the Johnson-Cook model, Johnson-Cook model gives sufficiently accurate results for most of the metallic materials like steel, tungsten, aluminum, copper etc. Since Al 7075-T651 is investigated in this thesis, it is decided to use the Johnson-Cook strength model to characterize Al 7075-T651 material. For this purpose, critical parameters of the Johnson-Cook strength model are obtained experimentally in this study.

Johnson and Cook [22] presented a constitutive model to define material characteristics in dynamic conditions such as high velocity impact, and explosive detonation in which materials are exposed to larger strains, high strain rates, and high temperatures.

In the study of Johnson and Cook, torsion tests at different strain rates, and dynamic Hopkinson bar tensile tests at different temperatures were used for twelve different materials such as OFHC Copper, Armco iron, 4340 steel etc. As a result of this study, a strength model was defined for the von Misses flow stress given by,

$$\sigma = [A + B\varepsilon^{n}][1 + Cln\dot{\varepsilon}^{*}][1 - T^{*m}] \tag{62}$$

where ε, $\dot{\varepsilon}^*$,T^* are equivalent plastic strain, dimensionless plastic strain rate, and homologous temperature, respectively. *A, B, C, n,* and *m* are the material constants. *A* is the yield stress at reference strain rate, *B* is the strain hardening constant, *C* is the strain rate constant, *n* and *m* are exponents of strain hardening and thermal softening, respectively. ε^* and T^* are dimensionless variables given by Equations (63) and (64).

$$\dot{\varepsilon}^* = \frac{\dot{\varepsilon}}{\dot{\varepsilon}^0} \tag{63}$$

$$T^* = \frac{T - T_{room}}{T_{melt} - T_{room}} \tag{64}$$

In these equations, $\dot{\varepsilon}$ is strain rate, $\dot{\varepsilon}^0$ is 1.0 s^{-1}, T_{room} is the room temperature, and T_{melt} is the melting temperature of the material.

The test data in this study were obtained from the torsion tests conducted over a range of strain rates between quasi static and 400 s^{-1}. Also, Split Hopkinson Bar system was used for the tensile test in a certain temperature range.

The test data obtained from Hopkinson bar tests at different temperatures by keeping the strain rates almost constant are given in Figure 25 for materials OFHC Copper, Armco iron, and 4340 steel. Results presented in Figure 25 show that with the increase of the temperature yield strength of the materials decrease.

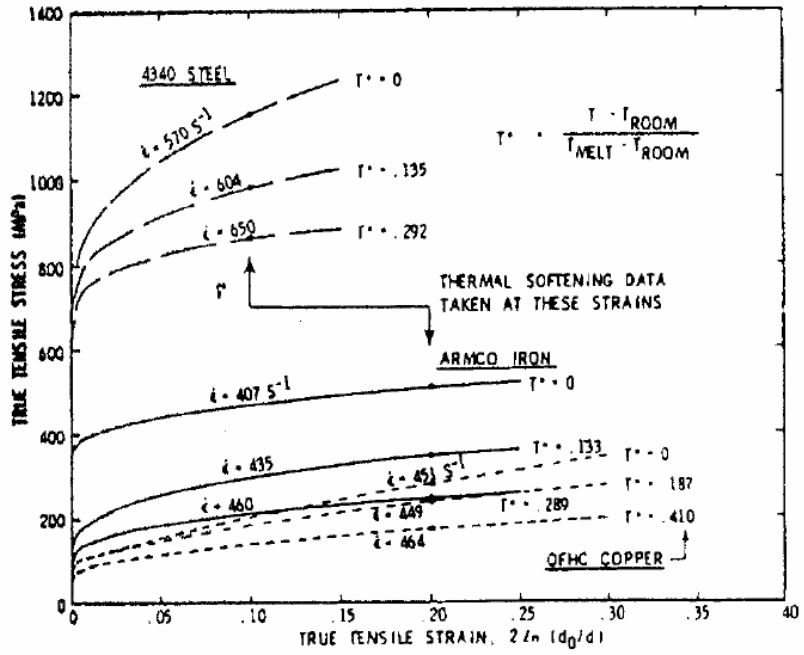

Figure 25 True Stress vs. True Strain Data obtained from Hopkinson Bar Test at Different Temperatures [22]

To observe the effect of the strain rate on the yield strength, torsion and tensile test were performed at the constant temperatures for the twelve materials. The results for OFHC Copper, Armco iron, and 4340 steel are given in Figure 26. For all of the materials, increase of the strain rate caused increase of the yield strength.

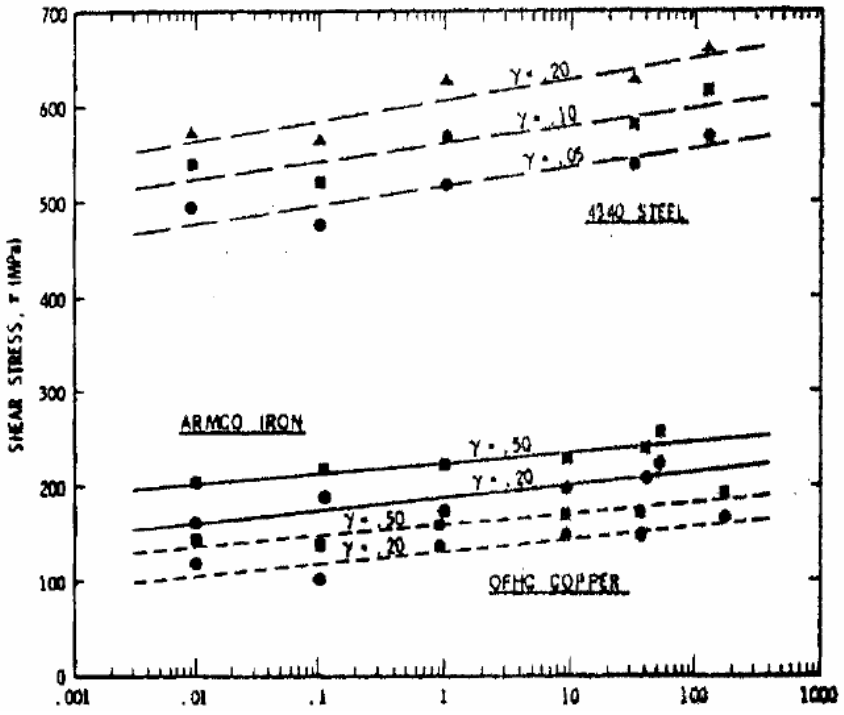

Figure 26 True Stress vs. True Strain Data obtained from Hopkinson Bar Test at Different Temperatures [22]

Johnson-Cook strength model is simple stress-strain model to describe the behavior of materials under different conditions. The constants used in the yield stress expression are obtained experimentally. In Table 2, Johnson-Cook parameters of OFHC Copper, Armco iron, 4340 steel are presented. These parameters are obtained by the tests conducted by Johnson and Cook [22].

Table 2 Johnson-Cook Parameters of OFHC Copper, Armco Iron, 4340 Steel [22]

Materials	A [MPa]	B [MPa]	n	C	m
OFHC Copper	90	292	0.31	0.025	1.09
Armco Iron	175	380	0.32	0.060	0.55
4340 Steel	792	510	0.26	0.014	1.03

Figure 27 shows the Johnson-Cook parameters in the Autodyn interface. Johnson-Cook parameters that are given as input are yield stress, hardening constant, hardening exponent, strain rate constant, and thermal softening exponent.

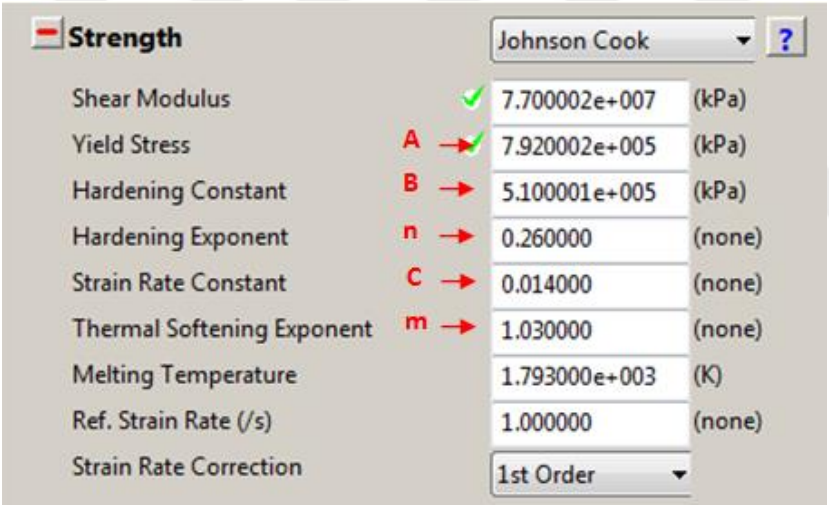

Figure 27 Johnson-Cook Parameters of 4340 Steel Strength Model in the Autodyn Interface [1]

2.3.2. Other Dynamic Strength Models

Johnson-Cook is a useful strength model for especially metallic type materials but other studies showed that there are other parameters affecting the yield strength. In this part, the most known dynamic strength models are summarized.

Zerilli and Amstrong [53] offered a dislocation-mechanics-based stress model for the materials by considering the effects of strain hardening, strain rate, and thermal

softening. This model also includes the behavior of body-centered- cubic (bcc) and face-centered-cubic (fcc) crystal structures and grain sizes unlike Johnson-Cook. To observe the effects of bcc and fcc, iron (bcc) and copper (fcc) metals were used in this study.

Mechanical Threshold Stress model [11], [14] uses the yield stress at 0 K as an internal state variable to describe the temperature independent deformations of the materials.

Steinberg and Lund [45] developed a constitutive model for yield strength from strain rates about 10^{-4} s^{-1} to 10^{6} s^{-1}. This model includes effects of temperature, pressure, shear modulus, work hardening, melting, Bauschinger effect, strain rate, and spall on the high deformation of the materials.

Another model offered by Preston, Tonks and Wallace [36] is applicable in the range of strain rates from 10^{-3} to 10^{12} s^{-1}. There are two main features of this model. One is that such a wide range of the strain rate was achieved by merging the flow properties of the metals in strong-shock-wave limit. Dislocation drag effects and thermal-activation regimes are considered being dominant on the yield stress. The second one is that the variables affecting the flow stress were scaled in the model. This model takes the microstructure of the materials into account since dynamic behavior of the material depends on the microstructural state like grain size and grain orientation distributions, dislocation density etc. Furthermore, anisotropy and grain alignment are neglected in the formulation.

CHAPTER 3

EXPERIMENTAL MEASUREMENT TECHNIQUES

3.1. Split Hopkinson Bar (Kolsky bar) Technique

Split Hopkinson Bar technique is a common method used for material characterization up to 10^3 strain rates. It is also called as Kolsky Bar since the final system was developed by Kolsky [27] although firstly offered by B. Hopkinson [19].

Split Hopkinson measurement technique has been developed as a consequence of studies and experiments conducted by scientists in different years. The studies were initiated by John Hopkinson. John Hopkinson loaded the free end of a wire which is fixed at the other end. By investigating the rupture point of the wire, the material behaviour was estimated [13].

Bertram Hopkinson [19] continued the experiments, and developed the pressure bar. Pressure bar measures the pressures of a projectile impacting a bar. To accelerate the projectile, or the bullet, high pressure generated by an explosive was used. At the end of the impacted bar, there is small rod which flies after the impact. The momentum of the flying piece was measured by a ballistic pendulum. The Hopkinson Pressure Bar was widely used to characterize the dynamic behaviour materials, and it has been continued to be modified by the future studies [13].

Kolsky [27] studied the dynamic behaviour of materials under high loading by the modified Hopkinson Pressure Bar which is shown in Figure 28. After this study, the technique has been called as *Kolsky Bar* or *Split-Hopkinson Pressure Bar* and today it is widely used to characterize the materials in dynamic conditions [13].

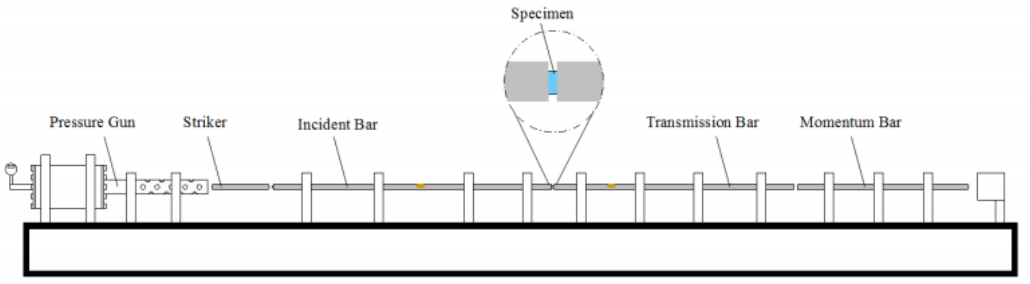

Figure 28 Schematic Represantation of the Typical Kolsky Bar [35]

Typical form of the Kolsky bar system that is currently used consists of a striker, incident, transmitter (or transmission), and momentum bars, a specimen, strain gages and data acquisition system. In this system, a striker is launched to impact the incident bar and upon impact it causes elastic wave propagation along the bar. Gas gun is widely used for this purpose due to being efficient, controllable, and safe. The elastic compressive wave begins propagating along the bar until the specimen which is placed between the incident and transmission bars. Due to impedance difference between the incident bar and the specimen, one part of the compressive pulse is transferred to the transmission bar along the specimen and the rest is reflected to the incident bar. To measure the elastic deformation, strain gauges are placed on the incident and transmission bars. These data are recorded by a data acquisition system such as an oscilloscope [35].

3.2. Photonic Doppler Velocimetry (PDV)

Photonic Doppler Velocimetry (PDV) is another technique used in the experiments to determine the dynamic behaviour of materials. This method was firstly developed by Strand et al (2006) and named as Heterodyne Velocimetry (HetV). In the following years, it was rendered as a compact and inexpensive system by recent developments [18].

In the heterodyne technique, laser is sent to the moving surface by a probe to measure the velocity of this surface. The information or the light is transported by optical fibers as shown in Figure 29 where f_0 is the emitted light frequency and f_d is the Doppler shifted light frequency [46].

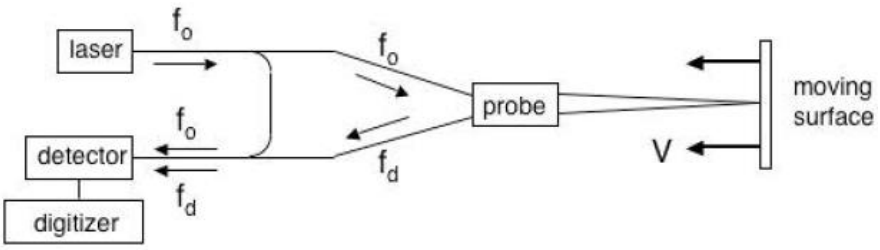

Figure 29 Basic Schematics of a PDV System [46]

Another term f_b is the beat frequency which is the magnitude of the difference between the emitted and the reflected (shifted) light frequencies given by Equation (65).

$$f_b(t) = |f_d(t) - f_0| \tag{65}$$

The beat frequency $f_b(t)$ is proportional to the moving surface velocity $v(t)$ as shown in

$$f_b(t) = 2\left[\frac{v(t)}{c}\right] f_0 \tag{66}$$

where c is the speed of light [46].

A full cycle of the beat signal corresponds to a distance half of the wavelength. In other words, velocity can be written in terms of the wavelength and the time of one cycle move as ,

$$v(t) = \frac{\lambda}{2P} \tag{67}$$

where λ is the wave length and P is the measured period of one cycle. As an example, in Figure 30, a laser having 1550 nm wavelength was used in the experiment [46].

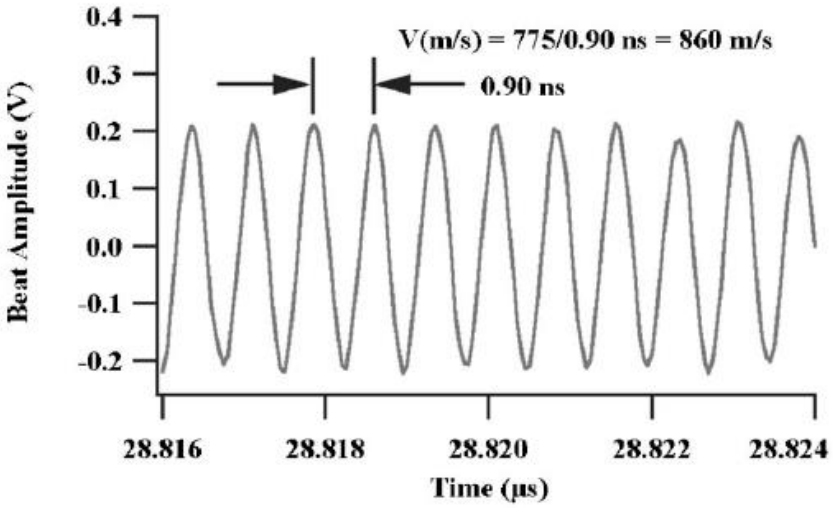

Figure 30 Beat Amplitude (V) Change in Time (μs) [46]

3.3. Velocity Interferometer System for Any Reflector (VISAR)

VISAR is a system which is commonly used with the modified Taylor impact test to measure the free surface velocity of the specimen during the test. The free surface velocity profile of the specimen is used to determine the dynamic behavior of materials. The velocity measurement is performed by sending a laser light beam towards to the specimen and using the reflected beam after some processes. To understand the VISAR measurement technique, underlying theories should be explained first.

Interferometry or *interferometer* which is derived from *interference,* is a technique based on the superposition of the waves. Mostly light waves or electromagnetic waves are used in common interferometers. According to the interferometry theory, when two light beams are superimposed, they may either reinforce or weaken each other and this is the basic phenomenon of interference [44].

Doppler Effect (Doppler shift) is another important phenomenon used in the VISAR system. Doppler Effect states that frequency of light waves is relevant for the relative motion between the wave source and the observer. The frequencies of waves increase, if the source and observer are approaching each other as shown in Figure 31 [6].

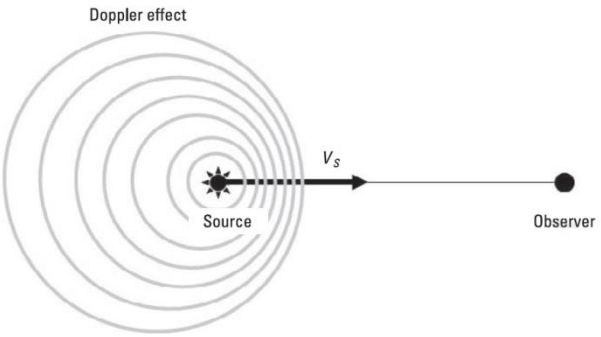

Figure 31 Doppler Effect [6]

VISAR technique was offered by Barker and Hollenbach [3] to measure the free surface velocity of the specimens by using interferometer and Doppler theories. The basis of this system is the Michelson Interferometer. The principles of VISAR are explained in this part by referring to the Michelson Interferometer which is a simpler technique on interferometry.

The Doppler Effect can be defined as the increase or decrease in frequency of a wave during the source motion toward or away from the observer. The frequency of the laser light is equal to ratio between the light speed *c* and the wavelength of the laser light λ as shown in Equation (68) [54].

$$v = \frac{c}{\lambda} \tag{68}$$

If there is a moving object with velocity *u* from which the laser light is reflected, the frequency of the reflected light *v'* can be written as,

$$v' = \frac{v}{1 \pm u/c} \tag{69}$$

where the minus (-) sign is used for objects moving towards the observer and the plus sign (+) is used for objects moving away from the observer. The change of the wavelength for the reflected light can be written as follows;

$$\Delta\lambda = \lambda' - \lambda = \pm\frac{\lambda}{c}u \tag{70}$$

Since there is a round trip distance in the Michelson Interferometer, the wavelength change can be defined as given in Equation (71).

$$\Delta\lambda = \lambda' - \lambda = \pm\frac{2\lambda}{c}u \tag{71}$$

In the Michelson Interferometer, the laser light path is given in Figure 32 where M_1 and M_2 are mirrors and BS is the beam splitter. Beam splitter has an angle of 45^o with respect to the incident laser beam. The incident beam is split into two beams. First one goes to the first mirror M_1 and reflects to the beam splitter BS and the second one goes to mirror M_2 and returns to the beam splitter. The reflected beams are split again by the beam splitter. And the part of the first beam reflected from M_1 and the part of the second beam reflected from the beam splitter are recombined by the beam splitter. The interferometry fringes are formed by this interference and they are detected by an observer or a detector [54].

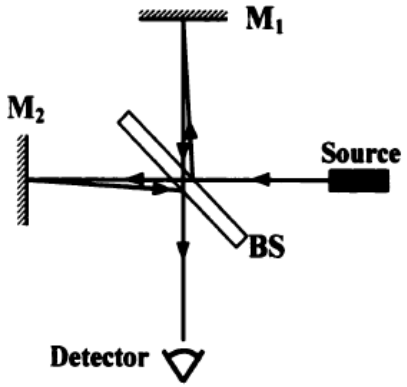

Figure 32 Schematic of Michelson Interferometer (M_1 and M_2 are mirrors and BS is the beam splitter) [54]

If two beams reflected from M_1 and M_2 have different frequencies, the beat frequency can be written by using the difference between them as shown in Equation (72). The

beat frequency is the only part of the intensity of light that can be detected by an oscilloscope [54].

$$\Delta v = v_1{}' - v_2{}' \tag{72}$$

If the beat frequency is zero ($\Delta v = 0$), no change is observed in the intensity of the light and the fringes are observed as static. If the two mirrors M_1 and M_2 have the same distance to the beam splitter, there will not be any difference in the frequencies of the lights then the fringes will be static. Even if the specimen has an acceleration or deceleration, it cannot be detected by the observer without a path length difference. If the mirrors are at different distances to the beam splitter, path length difference occurs between the beams. If the laser light reflects from an object having constant velocity even if there is a path difference, although Doppler shift effects are contained by laser light, the fringes will be static again. In the constant velocity, the frequencies are time-independent and there is no time delay in this case. However, if the object has acceleration or deceleration, the frequency will be a function of time. In this case, a delay occurs between the legs due to longer legs travelling in longer time compared to the shorter leg. Therefore, the beat frequency is not equal to zero and moving fringes can be observed. The velocity of the object can be calculated by using these fringes. From this discussion, it can be concluded that there are two cases needed for the velocity interferometer to be effective; leg length difference between the beams and an accelerated or decelerated motion of the object which causing the acceleration or deceleration in the fringe motion [54].

The delay time can be expressed by Equation (73) by using the length difference between two legs, Δx. Due to the reflection of light from the mirrors, the length is taken as $2\Delta x$ to represent the total path.

$$\tau = \frac{2}{c}\Delta x \tag{73}$$

If the two beams recombine with a delay time, the frequency difference will be as shown in Equation (74).

$$\Delta v = v_1'(t) - v_2'(t-\tau) \tag{74}$$

For constant wavelength, length difference between the legs, considering the round trip, can be written in terms of the wavelength λ as;

$$2\Delta x = N\lambda \tag{75}$$

where *N* is the number of waves and λ distance is the wavelength. Also, Equation (75) can be written in terms of the delay time τ as given in by Equation (76).

$$N\lambda = c\tau \tag{76}$$

The Equation (76) can be written as Equation (77).

$$N(t) = \frac{c\tau}{\lambda(t)} \tag{77}$$

Differentiating Equation (77) with respect to time *t*, Equation (78) is obtained.

$$\Delta N(t) = -\frac{c\tau}{\lambda^2}\Delta\lambda(t) \tag{78}$$

Substituting $-2\lambda u/c$ from Equation (71) in place of $\Delta\lambda$ in Equation (78) and solving it for the free surface velocity $u(t)$, one gets,

$$u(t) = \left(\frac{\lambda}{2\tau}\right)\Delta N(t) \tag{79}$$

$\Delta N(t)$ is replaced with *F(t)* which is the total amount of fringe at time *t* since the wave number cannot be count but the fringes can be observed. Also, the observed fringes do not give the velocity at the observation moment. Therefore, the specimen velocity can be written at time instance $(t - \tau/2)$ to consistent with the impact time by Equation (80).

$$u(t-\tau/2)=\frac{\lambda F(t)}{2\tau(1+\delta)} \tag{80}$$

where δ is the index refraction correction factor which is equal to zero if there is no a window material placed on the specimen's reflective surface.

By considering the Equation (80), it can be concluded that if the leg lengths are equal for the laser beams reflected from the mirrors, no velocity change is detected since the change is zero in the number of fringe. If the difference is not equal but small, it gives low velocity resolution since the observed fringes count decreases. If the length difference is long, high velocity resolution can be obtained due to higher number of fringes counted [54].

VISAR system is based on the theory of wide angle Michelson interferometer briefly mentioned above. A laser beam is sent to the surface of an accelerating specimen by VISAR and the beam reflects from the surface and returns to the system. By using beam splitters and etalons, a delay occurs between the split laser beams. This delay is used to find the acceleration of the object, and then the surface velocity profile is given as the output of the system.

CHAPTER 4

EXPERIMENTAL SETUP AND TEST RESULTS

4.1. Experimental Tools for High Strain Rate Material Characterization

4.1.1. VISAR

Working principles of VISAR and its properties are explained in Chapter 3. Fiber Doppler Velocity Interferometry (FDVI) is also a type of VISAR and this system is used during the experiments performed in the present study. This system is basically more compact type of classical VISAR measurement system.

4.1.1.1. Components of the FDVI

The FDVI system consists of several components which are the main chassis, four series G-photodetector modules, the experiment viewing probe and its optical cable, an IR sensitive card for viewing the 1550 nm laser beam. The components of the system are shown in Figure 33 [33].

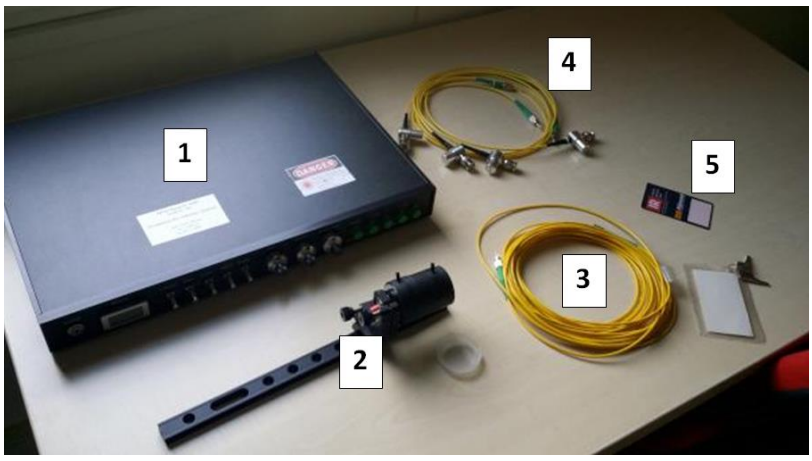

Figure 33 All Components of the FDVI System (main chassis (1), experiment viewing probe (2), the fiber cable (3), series G photodetector (4), IR sensitive card (5))

Main chassis is a black box consisting of the lasers, optical Erbium Doped Fiber Amplifier (EDFA), interferometer, interconnecting fiber optic cables, the battery pack and charger and control monitors. The battery can be charged by an AC power cord easily. The interferometer is controlled by several switches and knobs located in front of the main chassis. Main chassis also transmits the output signals to the data acquisition system (oscilloscope) by the series G photodetectors. The main chassis and all the components in it are shown in Figure 34.

Figure 34 Main Chassis

In the FDVI system, a laser beam is sent to the surface of the specimen and the reflected laser is collected by the experimental probe, shown in Figure 35. Experimental probe can move on a rail to adjust its position during the experiment. Experimental probe is connected to the interferometer by a fiber cable shown in Figure 35. Fiber cable is very long that the interferometer and the data acquisition system can be kept away from the experimental area.

Figure 35 Experiment Viewing Probe and the Fiber Cable

The optical signals of the interferometer are converted to electrical signals by photodetectors to view them in the data acquisition system. Figure 36 shows the photodetectors used. The interferometer and the data acquisition system are connected to each other by these cables. There are four outputs of the interferometer on the main chassis which are sin(+), sin(-), cos(+), cos(-). There are also four inputs of the data acquisition system to be connected to the interferometer [33].

Figure 36 Series G Photodetector

Laser light used in this system has a wavelength 1550 nm and this is not a visible light. Human eye can only see the light in the wavelength range of 380 nm and 750 nm. Lights having shorter wavelengths than the visible range are ultraviolet radiation, x-rays and gamma-rays, larger wavelengths are infrared radiation, micro waves and radio waves [6].

The laser of this system is in the category of infrared radiation (IR). Therefore, the system needs an IR sensitive card to make the laser light visible. Moreover, IR sensitive card is also useful to adjust and focus the experiment viewing probe correctly. Figure 37 shows the IR sensitive card that is part of with the system.

Figure 37 IR Sensitive Card (1550 nm)

4.1.1.2. Theory of Operation

As mentioned in section 3.3, the main purpose of the VISAR system is to determine the velocity of any moving surface by processing on the laser light beam sent to the moving surface and the reflected beam from the surface. In the FDVI system, experiment viewing probe (Figure 35) sends this beam as 1550 nm laser through an optical circulator and the reflected laser comes to this circulator again. This circulator sends the reflected light to the EDFA for amplification. Then, the amplified light comes to a delay leg interferometer. The basic principles of the interferometer are explained in section 3.3. The delay between the lights allows the velocity change of the surface of the specimen to be calculated. The sinusoidal light signals are converted to electronic signals to be monitored in the data acquisition system. Finally, the free surface velocity is calculated in a computer by using these converted signals. The schematic diagram of this system is given in Figure 38 [33].

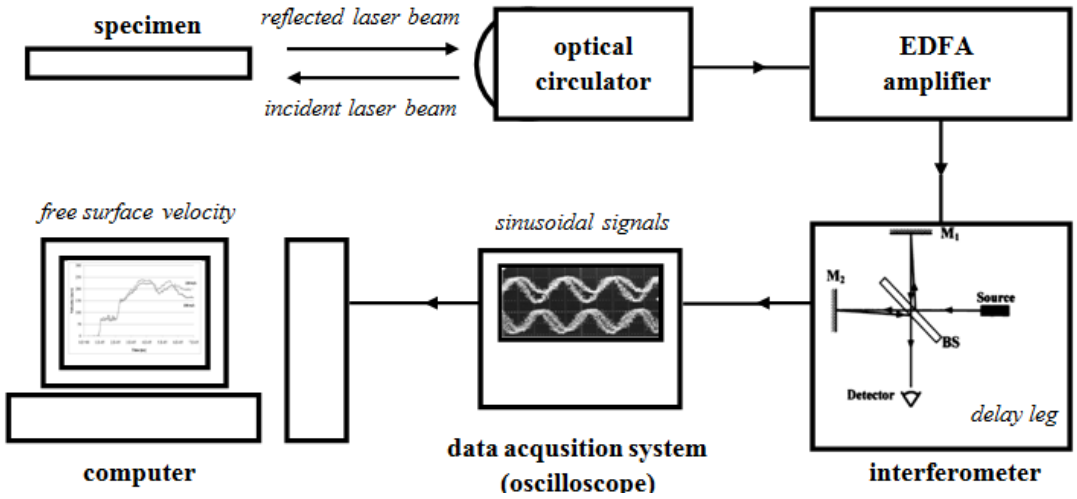

Figure 38 Simplified Schematic Diagram for FDVI (VISAR)

After the sinusoidal data is obtained from the data acquisition system, they should be converted to velocity by performing certain calculations. By using sine and cosine signals, velocity is calculated as given,

$$v(t) = v(0) + N(t)K_f + tan^{-1}\big(sin(t), cos(t)\big)K_f \qquad (81)$$

where *v(0)* is the initial velocity which is zero for this study since the specimen is stationary at the beginning of the test. *N* is the total number of fringes counted. Fringe defining one cycle of the light intensity is used to find the number of waves in the constant delay leg at any time. Sine and cosine parameters define the sinusoidal signals obtained by the FDVI. K_f is the fringe constant which determines the frequency change due to the Doppler shift. This constant can be calculated by ,

$$K_f = c\lambda_o/(2Ln_D) \tag{82}$$

where c is the speed of light , λ_o is the laser wavelength, n_D is index of refraction and L is the delay leg length [33]. Delay leg length defines the sensitivity of the measurement. According to the experiment type and sensitivity, the length value is selected. Table 3 represents delay leg length and the application areas with the time and velocity resolutions [33].

Delay leg length is a parameter of the fringe constant and it affects the velocity sensitivity. Velocity resolution depends on the fringe shift. Increase of the fringe shift causes higher velocity resolutions. Time resolution of system defines the measurement frequency of the interferometer. However, data acquisition system also should have enough resolution capacity [33].

Table 3 Time and Velocity Resolution Values for Some Applications [33]

L	K_f	V_{res}	T_{res}	Example Applications
10 mm	15 km/s/fr	20 m/s	50 ps	High Energy Density, Laser Effects, Exploding Foils
100 mm	1.5 km/s/fr	2 m/s	0.5 ns	Explosives, Shock Hydrodynamics, Space Debris
1 m	150 m/s/fr	0.2 m/s	5 ns	Interior Ballistics, Impacts, Damage Propagation
10 m	15 m/s/fr	0.02 m/s	50 ns	Acoustics, Machining, Material Science
100 m	1.5 km/s/fr	0.002 m/s	0.5 µs	Seismic Studies, Vibration, Motion Stability

The FDVI system used in this thesis has a delay leg of 1 m which is sufficient for impact type applications.

4.1.2. Data Acquisition System (Oscilloscope)

The FDVI needs a digital data acquisition system to collect data and a PC to process the data. In this test setup, a MDO3000 series digital oscilloscope, shown in Figure 39, is used as the data acquisition system. Oscilloscope has 4 analog channels, 500 MHz bandwidth, 2.5 GS/s sample rate, 10 M record length on all channels and these properties meet the FDVI requirements.

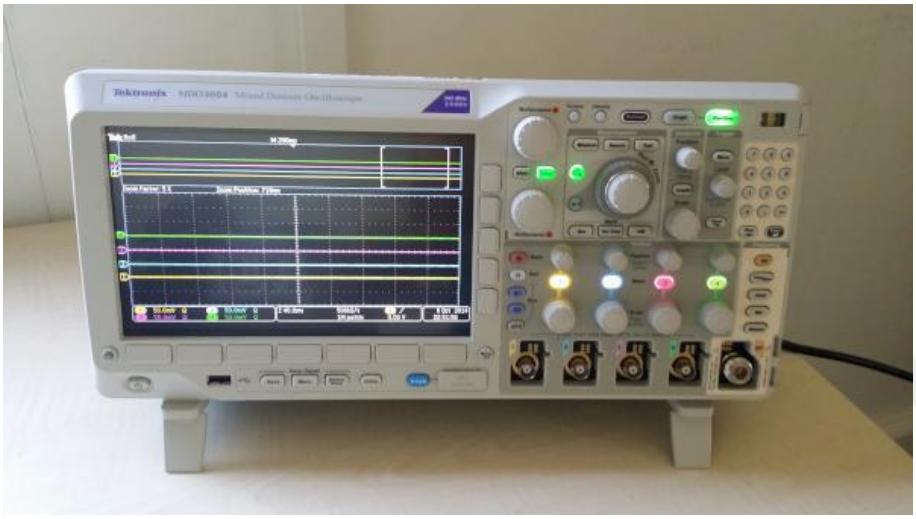

Figure 39 Digital Oscilloscope

The FDVI system operates continuously and it does not have a trigger to capture data during the test. Therefore, a trigger should be defined for the oscilloscope to stop the data flow and get the output data in desired range.

4.1.3. Gas Gun

Single stage gas guns basically consist of a gas reservoir and a barrel. Figure 40 shows schematic illustration of a single stage gas gun. The reservoir filled by high pressure of gas is opened to a small diameter barrel to launch the projectile. During the motion of the projectile in the barrel, the internal energy of the driving gas is progressively converted into kinetic energy. A part of this energy resides in the projectile and the

rest resides in the gas. As a first approximation, it can be stated that for a given initial internal energy, minimization of the kinetic energy of the driving gas maximizes the kinetic energy of the projectile. The kinetic energy that can be taken by a gas is directly connected to its molecular weight. Therefore, the use of a gas of low molecular weight, such as helium or hydrogen, seems to be the most appropriate choice [7]. Although hydrogen is considered the best choice among all gases in single stage gas guns due to its low molecular weight, it is not preferred in many cases since hydrogen is highly combustible. In single stage gas guns, helium and nitrogen are widely used gases since they are non-combustible and non-toxic.

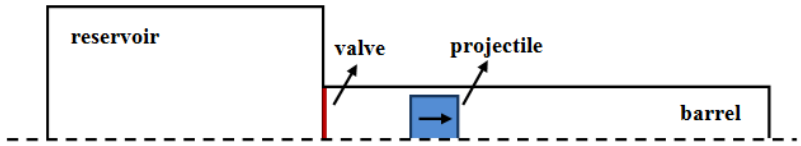

Figure 40 Schematic Illustration of a Single-Stage Gas Gun

For the purpose of the study conducted in this thesis, single-stage gas gun is sufficient for the projectile velocities less than 1000 m/s. In Figure 41, single-stage gas gun used in the experiments conducted in the thesis is shown. As shown in Figure 41, there is a reservoir at the back of the barrel where the high pressure gas is filled. After the projectile is placed at the inlet side of the barrel, the pressurized gas is released to accelerate it. Then, the accelerating projectile impacts the target placed in the cabin.

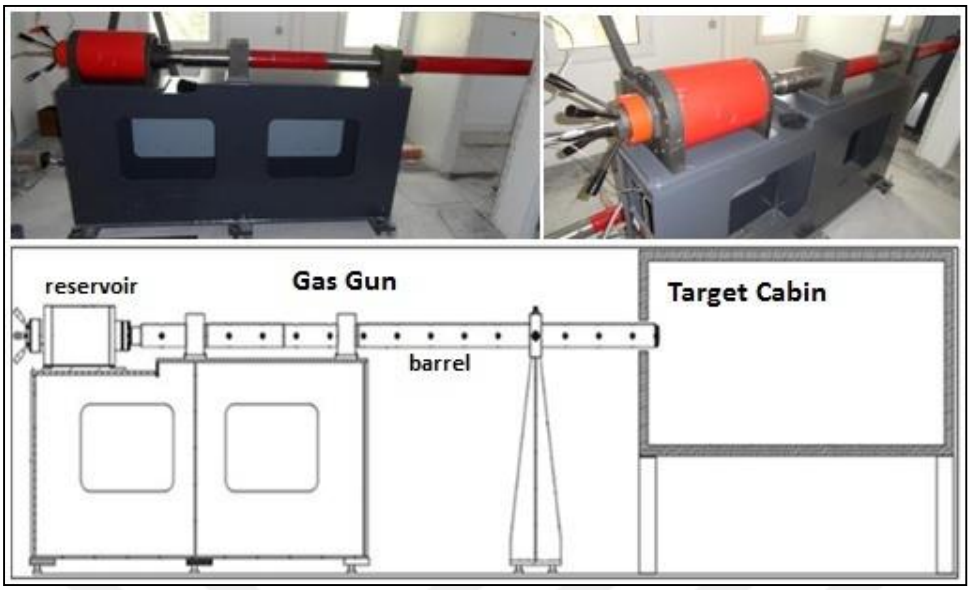

Figure 41 Single Stage Gas Gun Used in the Experiments

The gas gun used in the experiments within the scope of this thesis has a relation between gas type, gas pressure, weight and the outlet velocity of the projectile. By using the specimen weight and gas pressure for a certain gas, outlet velocity of the projectile can be predicted in the single stage gas gun system. For example, a specimen having 10 g weight can be accelerated to 400 m/s velocity by using approximately 100 bar nitrogen gas. If a heavier specimen is used for the same gas pressure, a lower specimen velocity will be obtained.

The outlet velocity is measured by a velocity measurement system next to the barrel exit. The outlet velocity is assumed as equal to the impact velocity for the test setup in this study since the sample is placed next to the velocity measurement device. In other words, the velocity measurement system is placed between the barrel exit and the test sample and there are several centimeters between the velocity measurement point and the impact point.

4.2. Material Characterization Tests for the Johnson-Cook Yield Stress Model

Johnson-Cook yield stress model is given in section 2.3.1. In the Johnson-Cook yield model there are five parameters (*A, B, C, n, m*) which completely define the model as given in Equation (83).

$$\sigma = [A + B\varepsilon^{n}][1 + Cln\dot{\varepsilon}^{*}][1 - T^{*m}] \tag{83}$$

To find these parameters, experimental techniques should be used like the tensile test and high strain rate tests such as the modified-Taylor impact test used in the present study. It should be noted that by the tensile and modified Taylor impact test, parameters of the Johnson-Cook yield model that can be determined are *A, B, C* and *n*. The *m* parameter in the model defines the temperature effect on the yield stress and to determine the parameter *m* additional experiments have to be performed at different temperatures. In the present study, since the material characterization tests are only performed at the room temperature, parameter *m* given in the literature for the test material is used to finalize the Johnson-Cook yield stress model.

In the thesis study, material characterization of Al 7075-T651 is conducted since it is a widely used material in aeronautical applications and TÜBİTAK SAGE projects. The temperature parameter of the Johnson-Cook yield model *m* is taken as 1.61 based on the available data in the literature [4], [23].

4.2.1. Tensile Test

Strength is one of the most significant properties for a material. Elastic and plastic deformation characteristics are mostly needed to define the material response to any loading. Yield point, ductility or material failure limit are some of the properties of a material that have to be determined to characterize the material. With the tensile test material characterization can be performed in quasi-static conditions.

Tensile test is based on uniaxial tensile loading of materials. The technique is used to determine the yield strength, yield point elongation, tensile strength, elongation and the reduction of area in the material [2].

4.2.1.1. Tensile Test Specimen Preparation

Tensile Specimen

Tensile test specimen is prepared as a cylindrical part which is in accordance with the E8M standard of ASTM (American Society for Testing Materials) [2]. E8M is applicable for the metallic materials in any form at room temperature. The standard diameter is 12.5 mm and the gage length for the elongation should five times the diameter. The dimensions and shapes of the specimens are defined in Figure 42 and Table 4.

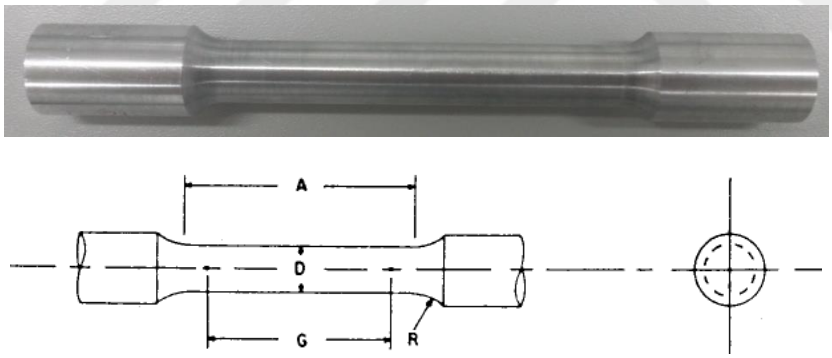

Figure 42 Tensile Test Specimen and Critical Dimensions

In Figure 42, *G*, *D*, *R* and *A* represent gauge length, diameter, radius of the fillet, and the length of reduced section, respectively. All dimensions and tolerances of the specimens are given in Table 4.

Table 4 Dimensions of Tensile Test Specimens

Critical Dimensions of Specimen	Dimension Symbols	Dimensions [mm]
Gauge Length	G	62.5±0.1
Diameter	D	12.5±0.1
Radius of Fillet, min	R	10
Length of Reduced Section, min	A	75

Test System

Tensile tests were performed by the electromechanic tensile testing machine Zwick/Roell Z100 with video extensometer as shown in Figure 43. Zwick/Roell Z100 testing machine can be used for materials between the room temperature and 1200ºC. Capacity of the test machine is 100 kN and the test rate can be between 0.0005 mm/min and 600 mm/min.

Figure 43 Tensile Test System

Extensometer is a device used for the measurement of length of an object. There are several types of the extensometers like contact, non-contact, laser, and video. Video extensometer performs this measurement by capturing images of the specimen during test using a frame grabber or a digital video camera. In the present study, video camera which is attached to a PC is used in the tests. The specimens are marked by special

stickers and video camera tracks the pixel distance between the stickers continuously during the tensile test. The resolution of the system is about micrometers and gives highly accurate results.

In the tensile tests, ISO 6892 was referenced for the testing speed [21]. There are two methods for specifying the testing speed in ISO 6892. Method A is based on strain rate and method B is based on stress rate. Method B is offered to minimize the measurement uncertainty of the test results. In the present study, strain rate for the determination of the tensile strength is taken as 0.0067 s^{-1} which is acceptable by ISO 6892. Strain rate of 0.0067 s^{-1} corresponds to a test speed of 25 mm/min for the Al 7075-T651 used in the experiments. It should be noted that in the present study, it is aimed to obtain the stress-strain relation at any strain rate below the high speed ranges. Thus, the change of yield stress could be found in different strain rates. The selection of strain rate of 0.0067 s^{-1} is considered to be low enough for the determination of the yield stress in quasi-static conditions. The elongation and strain are measured by the video extensometer by tracking the reference points on the test samples. To obtain the true stress-strain curve, the change of sample diameter is also measured by the video extensometer.

4.2.1.2. Tensile Test Results

To define the yield stress, Johnson-Cook model has five parameters, which are *A* (yield strength), *B* (hardening constant), *C* (strain rate constant), *n* (hardening exponent), and *m* (thermal softening exponent). *m* parameter is not included in this study as mentioned before. Tensile test results are used to obtain *B* and *n* parameters. Also, by using these results in a combination with the modified Taylor impact test results, *A* and *C* constant are calculated.

Tensile test results are given in Figure 44 as the true stress-true strain curve for the Al 7075-T651 material. Yielding begins at about 540 MPa and the stress continues to increase in the plastic region for tensile tests conducted at 0.0067 s^{-1} strain rate.

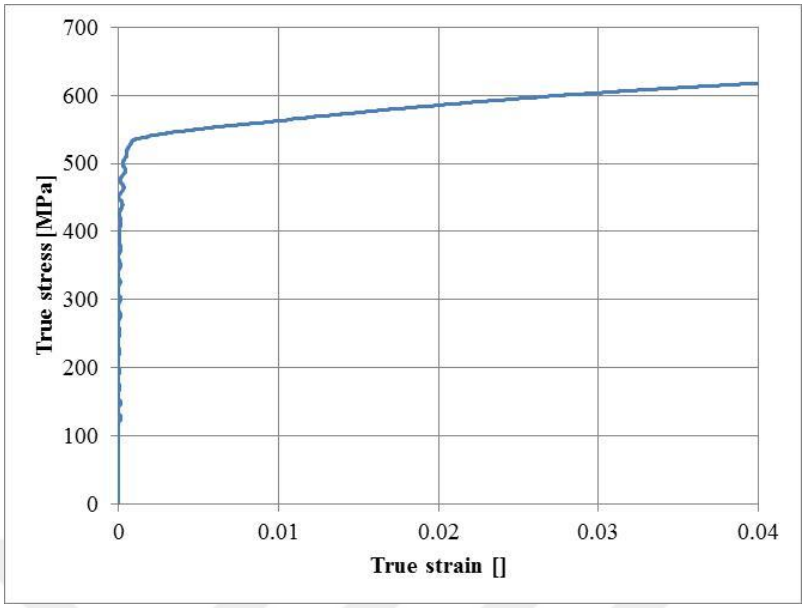

Figure 44 True Stress-Strain Curve of Al 7075-T651

The curve in Figure 44 should be defined with three parameters for the Johnson-Cook model. Therefore, a curve is fit to the experimentally determined stress-strain curve to obtain an analytical expression. The stress-strain curve fit for the Al 7075-T651 in quasi-static condition is given in Equation (84). Equation (84) gives the fit in the plastic region since the plastic region is important for the material characterization.

$$\sigma = 540 + 680\varepsilon^{0.63} \tag{84}$$

Figure 45 shows the test results and the curve fit in the plastic region. While obtaining Equation (84), elastic region of the stress-strain curve is not considered, as mentioned above. Yield point is assumed as 540 MPa to match the test results. Then, the other parameters are arranged by trial and error so that the curve fit matches the experimentally determined stress strain curve closely.

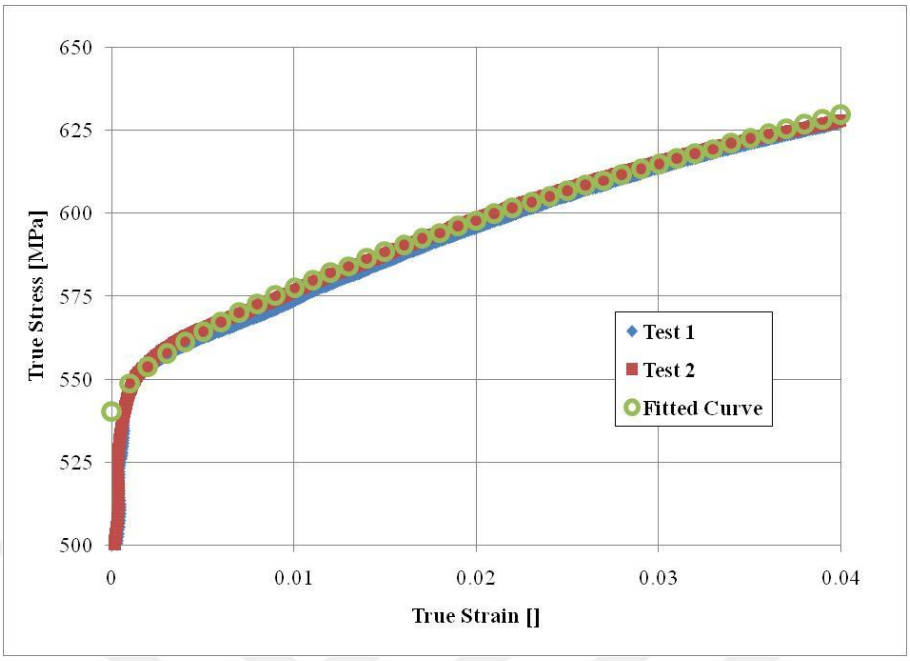

Figure 45 True Stress-Strain Curve of Al 7075-T651 in Plastic Region and the Curve Fitting

4.2.2. Modified Taylor Impact Test

In tensile tests, *B* (hardening constant) and *n* (hardening exponent) parameters are defined but to calculate the *A* (yield strength) and *C* (strain rate constant) parameters, modified Taylor impact test results should be used in addition to tensile tests. Modified Taylor impact test is based on measuring the free surface velocity of a sample impacted by a projectile. In the following, modified Taylor impact test set-up is introduced and experimental results are presented.

4.2.2.1. Preparation of the Experimental Set-up

Projectile and the Test Specimen

In the present study, a gas gun having a 25 mm barrel bore diameter is used to accelerate the projectile. Therefore, to accommodate the projectile, a sabot with 25 mm outer diameter, and a 20 mm diameter projectile are designed. The projectile is made of X153CrMoV12 steel (63 HRC) to prevent the plastic deformation of the

projectile during the impact event. The test specimen material, for which the material characterization is performed, is made of Al 7075-T651 and it has 5 mm diameter and 50 mm length. With these dimensions, aspect ratio of the test specimen is 10 which is the acceptable value for the 1-D wave propagation assumption to be valid [39]. The manufactured test specimen, projectile and sabot are shown in Figure 46.

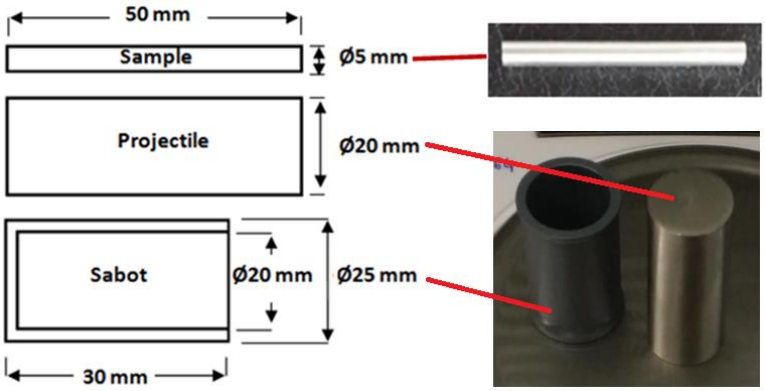

Figure 46 Modified Taylor Impact Test Specimens and Their Dimensions

VISAR Setup

VISAR system's theoretical specifications and working principle are explained in section 3.3 in detail. The system has a cable for the data transfer with the experimental viewing optic and four cables between the main chassis and the oscilloscope. The experiment viewing probe is fixed in the test cabin in a protective case but the main chassis and the oscilloscope are located on a table outside the cabin. Figure 47 shows the main chassis of VISAR and oscilloscope connections.

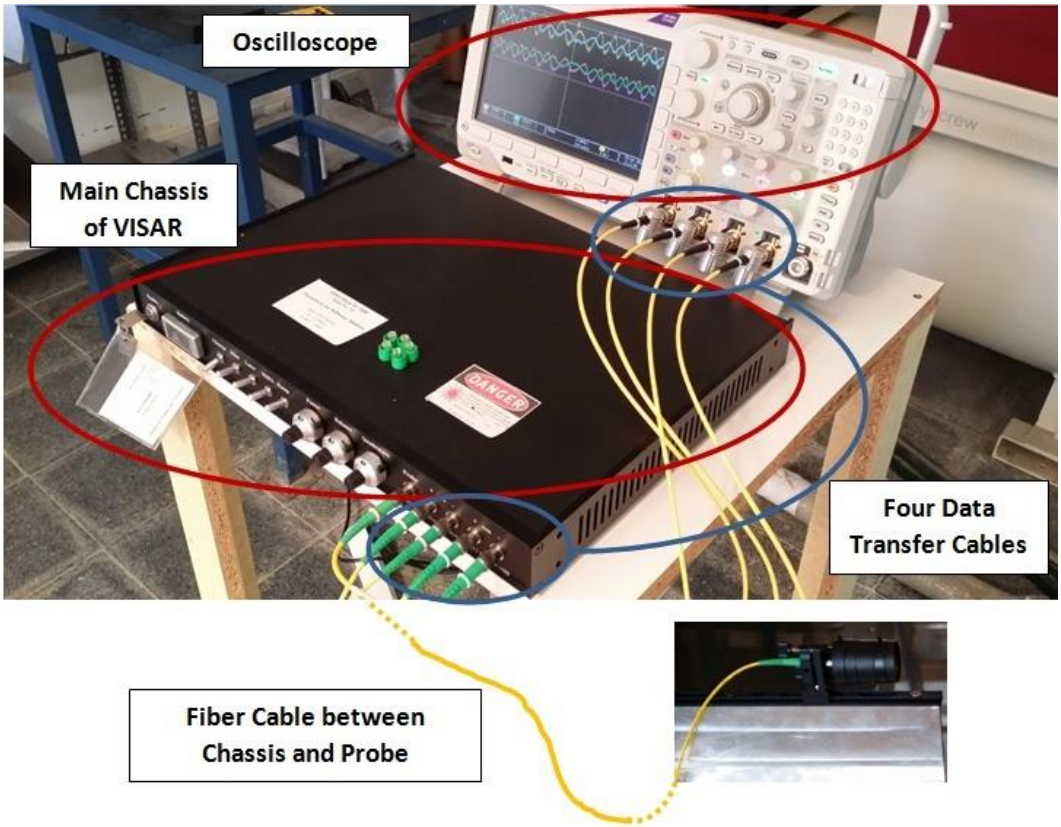

Figure 47 Main Chassis of VISAR and Oscilloscope Connections

Experimental Setup

The experimental setup of the modified Taylor impact test and VISAR system are shown in Figure 48. To explain the system more clearly, it is separated into two parts as the first part of the test setup and the second part of the test setup. The first part of the test system is shown in the right side of the system in Figure 48. The first part of the test system covers the beginning of the exit of the projectile from the barrel until it impacts the test sample. The second part of the test system is shown in the left of the system in Figure 48 covers the impact event and measurement by the VISAR system and completion of the data record.

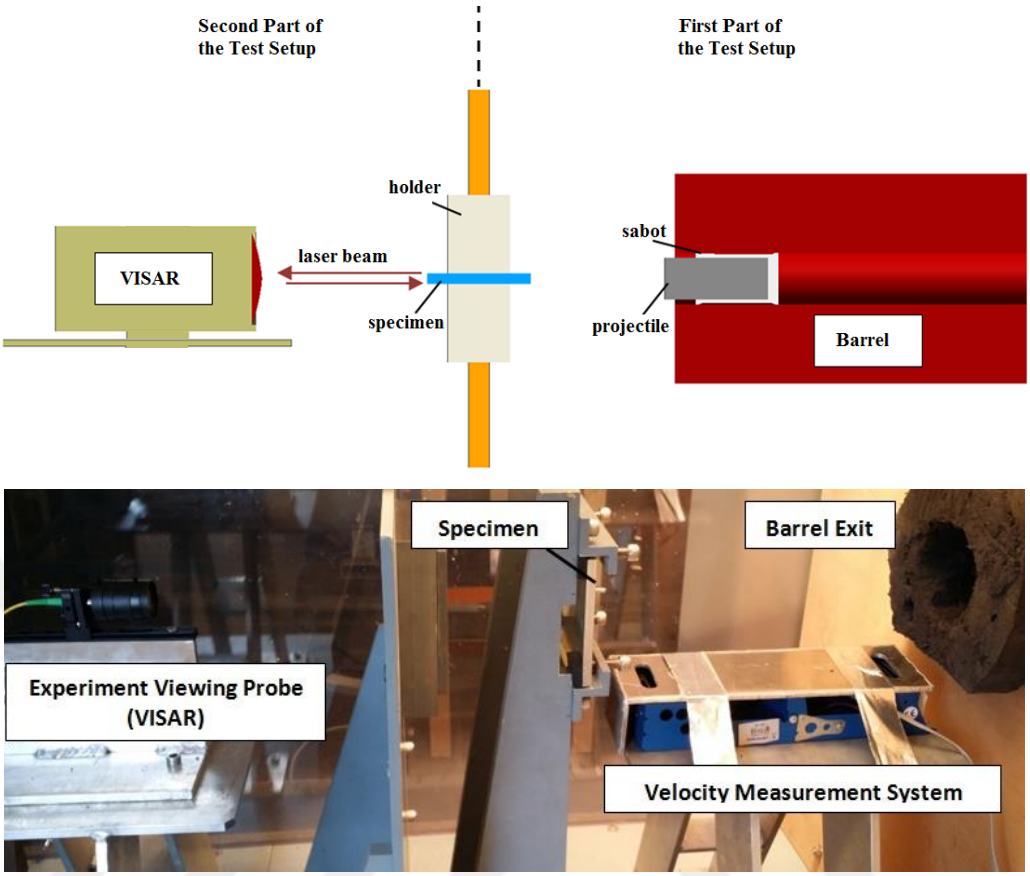

Figure 48 Modified Taylor Impact and VISAR Experimental Test Setup

In the first part of the experimental setup, the test specimen is located in front of the barrel exit as shown in Figure 49. Test specimen is fixed by the cylindrical foam to avoid the effects of the holder on the stress waves. Projectile velocity is measured by a velocity measurement system between the barrel exit and the test specimen. This system named as *Chrony* can measure the velocity up to 2000 m/s with a high accuracy. Chrony has two eyes located in each of the plastic housings at the front and back of the main unit. They are located under twin lenses at the bottom of these housings and they detect the passage of a bullet over them by sensing the change in the amount of light. In other words, they detect a momentary change in the light density. As the bullet passes over the first detector, it trips a counter, which begins to count very rapidly. The counter is shut off by the second photo sensor when the bullet passes over it. The computer in Chrony converts the information into meters per second. The case covering the system was manufactured by aluminum to protect the

Chrony from the damages. The projectile is launched from the barrel at a certain velocity and it impacts the sample in this part of the test system. Then, the sample begins to move in the impact direction.

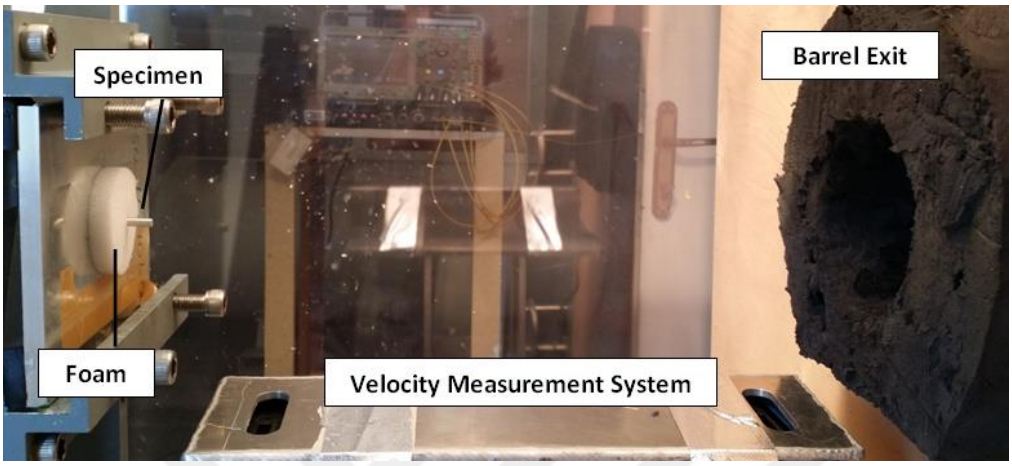

Figure 49 First Part of the Test System (Front Side of the Specimen)

The second part of the test system includes the sample and the experiment viewing probe as shown in Figure 50. There is a wall with a hole between the sample and the probe. The hole in the wall just allows the laser beam to pass to reach the back surface of the test specimen. But the wall also prevents the sample and projectile reaching the probe. There is also a second Chrony measuring the impacted specimen velocity. In this case, Chrony was not placed to the bottom of the specimen as the first one; it was placed to the left of the specimen moving direction. So, it is not covered in Figure 50. The probe is also protected by a case from the outside effects which may occur due to the impact phenomenon. Free surface velocity of the moving test specimen is measured by the VISAR in this part of the system.

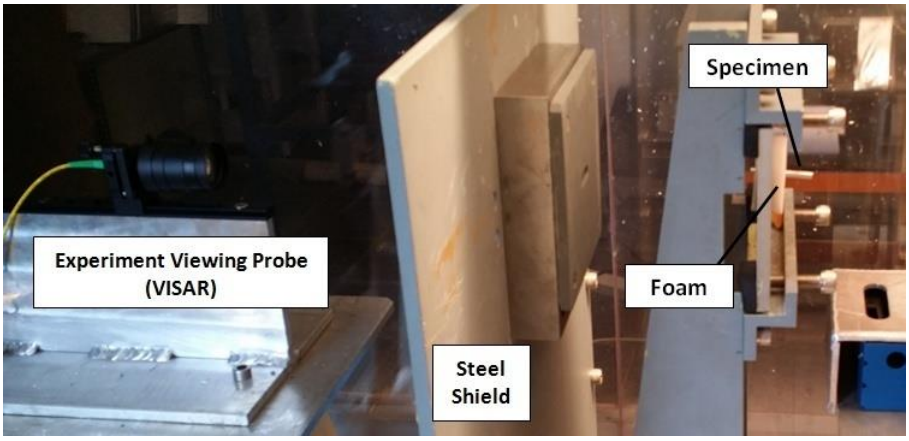

Figure 50 Second Part of the Test System (Rear Side of the Specimen)

4.2.2.2. Test Results

The experiments are conducted with a velocity 180 m/s and 196 m/s for the projectile and the free surface velocity profiles obtained are shown in Figure 51. The final velocities of the specimens were measured as 206 m/s and 220 m/s respectively by another velocity measurement system (Chrony) which is the same system used at the measurements of the specimen velocity at the barrel exit. It should be noted that even if the impact test is conducted by different velocities of the projectile and different velocities are obtained for the test sample, the velocity increase profiles are very similar with each other as shown Figure 51. All curves clearly have stepwise increase due to reflection of the elastic wave from the rear side of the specimen.

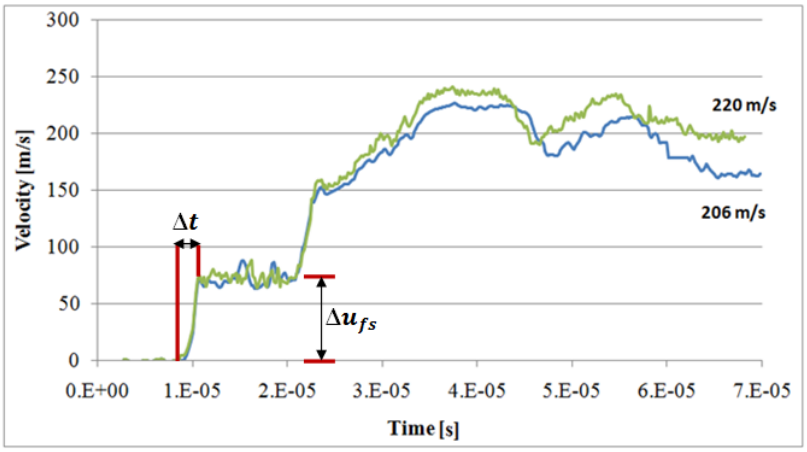

Figure 51 Free Surface Velocity Profile of the Impacted Samples

Velocity at the free surface of the specimen increases from zero to a certain value due to elastic wave reflection, then the velocity remains constant until the next elastic wave propagation. The velocity increase at each reflection of the elastic wave is defined as the free surface velocity. According to Figure 51, the first step of the velocity profile is from 0 m/s to 71 m/s. The velocity fluctuates around between 60 m/s and 80 m/s, and the average velocity in this range is calculated as 71 m/s. So the free surface velocity for Al 7075-T651 is taken as 71 m/s. Moreover, the duration of the velocity increase is another important value given in Figure 51. The strain rate will be calculated by using the time change during the velocity increase. From Figure 51, the change in time Δt was determined as 1.4×10^{-6} s.

Modified Taylor impact test is the reverse of the classical Taylor impact test, as mentioned before. In the modified Taylor impact test, a rigid projectile impacts the sample instead of impacting the sample to a rigid body. However, in both tests deformation of the test sample is similar. For the first test having the final velocity of 206 m/s, the initial and the final dimensions of the length and the diameter of the specimen are measured by the caliper as shown in Figure 52. There is a buckling on the specimen length since the specimen impacts the wall after accelerated by the projectile.

Figure 52 Initial and Final Dimensions of the Sample (for the sample having final velocity 206 m/s)

The changes in the dimensions are given in Table 5. As shown in the table, the length of the specimen decreased and the impact surface enlarged due to plastic deformation. It should be noted that in Table 5, diameter change is given for the surface impacted by the projectile. The diameter of the other end of the specimen remains constant since the plastic waves could not reach to the other end of the sample.

Table 5 Initial and Final Dimensions of the Sample (for the sample having final velocity of 206 m/s)

Dimensions	Initial	Final	Change [%]
Diameter [mm]	5.09	5.87	15.3%
Length [mm]	50.03	46.79	-6.5%

CHAPTER 5

MATERIAL CHARACTERIZATION AND VALIDATION STUDY

5.1. Material Characterization by Test

In this thesis, parameters of the Johnson-Cook dynamic strength model of Al 7075-T651 are obtained experimentally. Tensile tests and modified Taylor impact tests are conducted to determine the Johnson-Cook material model parameters of Al 7075-T651. Johnson-Cook model has five constant parameters, *A* (yield strength), *B* (hardening constant), *C* (strain rate constant), *n* (hardening exponent), and *m* (thermal softening exponent) which have to be determined to predict the behavior of the material in dynamic loading conditions. This model is defined again in Equation (85).

$$\sigma = [A + B\varepsilon^{n}][1 + Cln\dot{\varepsilon}^{*}][1 - T^{*m}] \tag{85}$$

B and *n* parameters are obtained directly by the tensile tests. However, *A* and *C* parameters can only be determined by using the tensile test results and the modified Taylor impact test results together. In this part, the results of tensile tests and modified Taylor impact tests are presented along with the calculations and the methods in order to determine the *A* and *C* parameters of the Johnson-Cook model. Since *m* is the thermal softening parameter and this study does not cover the experiments for this constant, parameter *m* is determined from the literature as 1.61.

Yield strength is related with elastic wave speed, density and free surface velocity profile of a material as mentioned in section 2.2.3. Density and elastic wave speed in Al 7075-T651 are given in Table 6. Free surface velocity change was measured by Modified Taylor Tests as explained in section 4.2.2.2. The free surface velocity profile increases step by step due to elastic wave behavior. Each reflection of the elastic wave from the free surface during the propagation causes increase of velocity. Until the next

turn, the velocity oscillates around a constant velocity. In this study, this velocity change was determined as 71 m/s for Al 7075-T651.

Table 6 Material Properties for Aluminum 7075-T651

Material Properties	Aluminum 7075-T651
Reference Density	2810 kg/m^3
Shear Modulus	26.9 GPa
Bulk Sound Speed	6300 m/s
Melting Temperature	893 K

Yield stress is calculated by elastic wave speed, density and free surface velocity utilizing Equation (86).

$$\sigma_{yd} = \frac{1}{2}\rho c_L \Delta u_{fs} = \frac{1}{2}(2810)(6300)(71) = 628\ MPa \tag{86}$$

where the stress σ is the yield stress, ρ is density, c_L is elastic wave speed, the free surface velocity Δu_{fs} is the velocity change at the back surface of the rod.

The strain in this event can be written as given in Equation (87).

$$\varepsilon = \frac{\Delta u_{fs}}{2c_L} = \frac{71}{2(6300)} = 5.635x10^{-3} \tag{87}$$

The strain rate is calculated by using derivative of strain with respect to time as shown in Equation (88).

$$\frac{d\varepsilon}{dt} = \frac{\varepsilon}{\Delta t} = \frac{5.635x10^{-3}}{1.4x10^{-6}} = 4025\ s^{-1} \tag{88}$$

The yield stress is calculated as 628 MPa for the given values of density (2810 kg/m^3) and elastic wave speed (6300 m/s) given in Table 6 and free surface velocity (71 m/s)

measured by VISAR in modified Taylor impact test. Then, the strain is calculated as $5.6x10^{-3}$ by using elastic wave speed and free surface velocity according to Equation (87). The Equation (88) gives the calculation method of strain rate for this experiment. Time change Δt was measured as $1.4x10^{-6}$ s as shown in Figure 51 in section 4.2.2.2. Finally, the strain rate is calculated as 4025 s^{-1}. As a result, at 4025 s^{-1} strain rate, the yield stress of Al 7075-T651 is defined as 628 MPa. Table 7 summarizes the dynamic material data obtained by the Modified Taylor Impact Test.

Table 7 Dynamic Material Data obtained by the Modified Taylor Impact Test

v_{final} [m/s]	u_{fs} [m/s]	u_p [m/s]	σ_y [MPa]	ε [$x10^{-3}$]	$\dot{\varepsilon}$ [s^{-1}]
206	71	35.5	628	5.63	4025

Utilizing the yield stresses which are 540 MPa and 628 MPa at 0.0067 and 4025 s^{-1} strain rates respectively, a linear logarithmic relation between stress and strain rate can be constructed as shown in Figure 53.

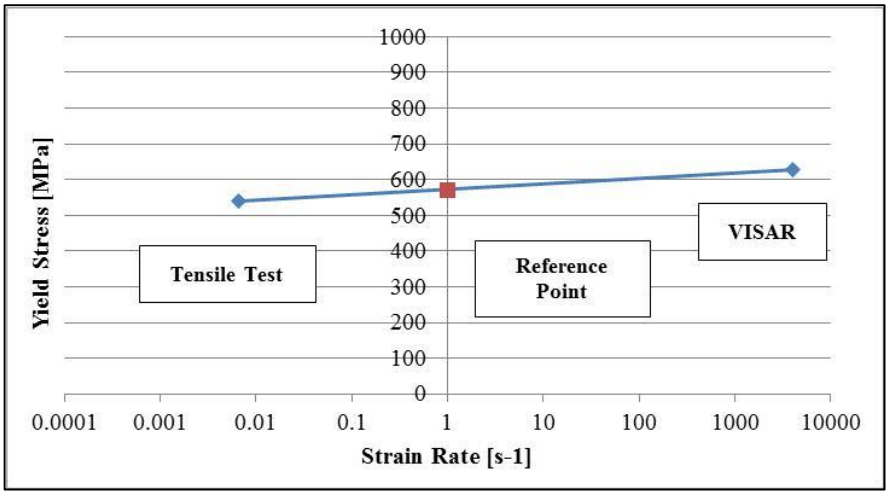

Figure 53 Yield Stress-Strain Rate Change of Al 7075-T651

By using two points as shown in Figure 53, the yield strength at reference strain rate 1.0 s^{-1} which is *A* parameter of the Johnson-Cook model and the slope of the yield

stress strain rate curve which is the *C* parameter of the Johnson-Cook model should be calculated. To clarify the calculations, firstly recall the Johnson-Cook equation as given in Equation (85).

Johnson-Cook model consists of three parts which are strain, strain rate and thermal parts. All the test in this study was conducted in room temperature and thermal part of the equation will be 1.0 due to T^{*m} is equal to zero at room temperature. The Equation (85) can be written as Equation (89) without thermal term.

$$\sigma = [A + B\varepsilon^{n}][1 + Cln\dot{\varepsilon}^{*}] \tag{89}$$

In the first term of the Equation (89), A gives the yield stress and $B\varepsilon^{n}$ gives the strain hardening effects which shows the stress behaviour above the yield point. Since the stress is investigated at yield point, the strain hardening effects are neglected and $B\varepsilon^{n}$ term is taken as zero. The Equation (89) can be written as Equation (90).

$$\sigma = [A][1 + Cln\dot{\varepsilon}^{*}] \tag{90}$$

Equation (90) is written for the low strain rate and high strain rate conditions as given in Equation (91) and Equation (92) respectively.

$$540 = [A][1 + Cln(0.0067)] \tag{91}$$

$$628 = [A][1 + Cln(4025)] \tag{92}$$

By solving the Equation (91) and Equation (92), parameter *C* of the Johnson-Cook model is calculated as 0.011 and the parameter *A* of the Johnson-Cook model is calculated as 570 MPa. The reference strain rate is taken as 1.0 s^{-1} which makes $Cln\dot{\varepsilon}^{*}$ term zero and the yield stress occurs equal to *A* parameter. The reference strain rate (1.0 s^{-1}) and *A* parameter (570 MPa) indicate a point at yield stress-strain rate curve and *C* parameters define the slope of this linear curve. Johnson-Cook parameters of Al 7075-T651 material obtained by the tensile test (*A, B, C, n*), Modified Taylor Impact Test-VISAR (*A, C*) and from the literature (*m*) are given in Table 8.

Table 8 Johnson-Cook Constitutive Parameters of Al 7075-T651

Yield Strength, A [MPa]	Hardening Constant, B [MPa]	Hardening Exponent, n	Strain Rate Constant, C	Thermal Softening Exponent, m
570	680	0.63	0.011	1.61*

*Taken from [4], [23]

The values in Table 8 are used in the formulation of the Johnson-Cook yield stress model in Equation (93).

$$\sigma_{AL7075-T651} = [570 + 680\ \varepsilon^{0.63}][1 + 0.011\ln \dot{\varepsilon}^{*}][1 - T^{*1.61}] \qquad (93)$$

5.2. Comparison of the Modified Taylor Impact Test Results with the Simulation Results

Johnson-Cook model of Al 7075-T651 is defined by using experimental results obtained in tensile and VISAR tests. However, the parameters should be verified by simulation results. Therefore, an Autodyn simulation is conducted such that in the analysis model experimentally determined parameters of the Johnson-Cook yield strength model are used. In Figure 54, parameters of the Johnson-Cook yield strength model are shown in the Autodyn interface.

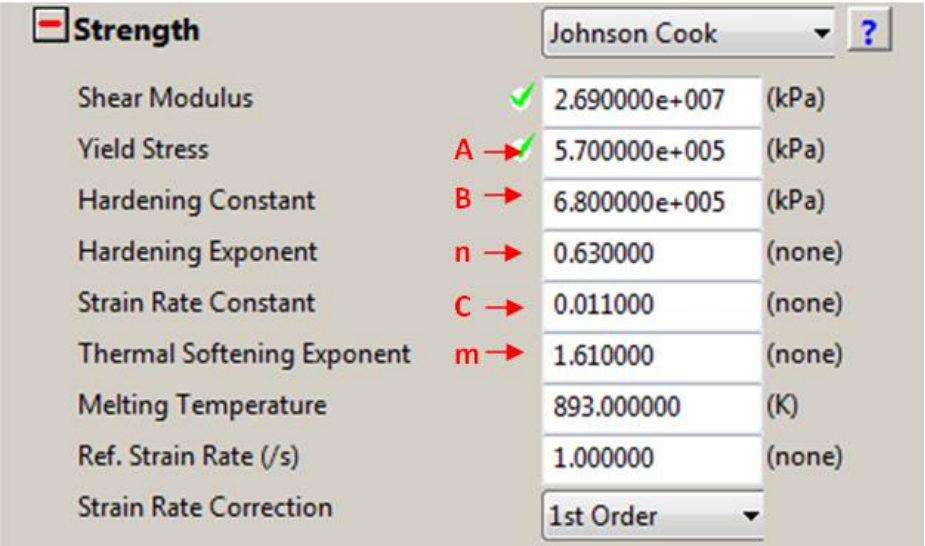

Figure 54 Material Properties of Al 7075-T651 Obtained Experimentally Given as Input to Autodyn [1]

For the simulation, 2D axially symmetric impact simulation including the projectile and the sample model is prepared. Figure 55 shows the axially symmetric Autodyn model used in the simulations. The sample is a cylindrical rod having 5.09 mm diameter and 50.03 mm length to be consistent with the test, and the projectile is a cylindrical rod having 20 mm diameter and 50 mm length.

Since the free surface velocity is important in this analysis, a gauge point is added to the end of the sample to capture the free surface velocity, as shown in Figure 55. This gauge records the free surface velocity history. Normally, the history file shows the average velocity for whole the sample but by adding a gauge point, point velocity at the center of the free surface can be recorded. In the simulation, an initial velocity as 180 m/s is defined for the projectile.

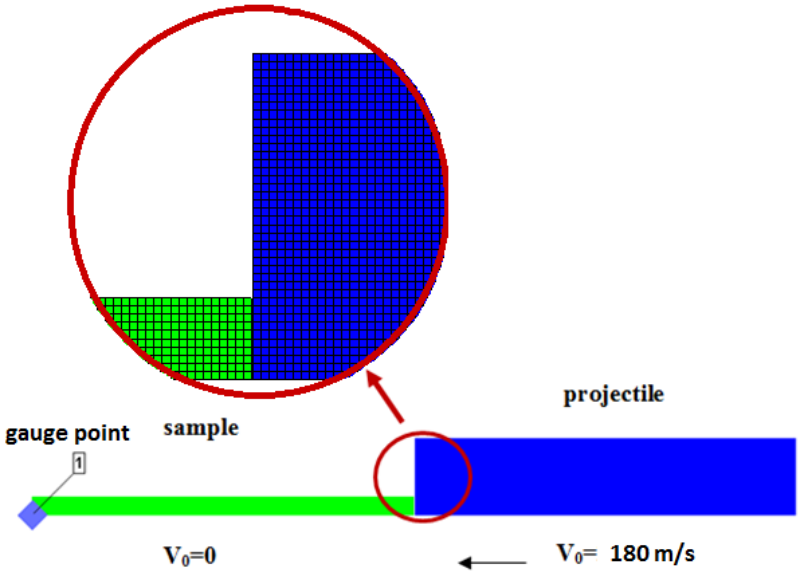

Figure 55 2D Axially Symmetric Autodyn Model for Simulations

Mesh size is defined as 0.25 mm to obtain sufficiently accurate results. The preliminary Autodyn studies are conducted with 0.5 mm, 0.25 mm and 0.1 mm mesh sizes and velocity data is obtained as shown in Figure 56. In Figure 56, it is seen that

when the mesh is made finer, fluctuations occur in the free surface velocity profile in the constant speed regime. Coarser mesh (0.5 mm) eliminates velocity fluctuations. However, in the experiments, the oscillations are observed and the fluctuations are not desired to be eliminated. Therefore, mesh size is made finer (0.25 mm) to capture the velocity oscillations. Since the simulations performed by the 0.1 mm mesh size took longer time unnecessarily, 0.25 mm mesh size is used in the Autodyn simulations.

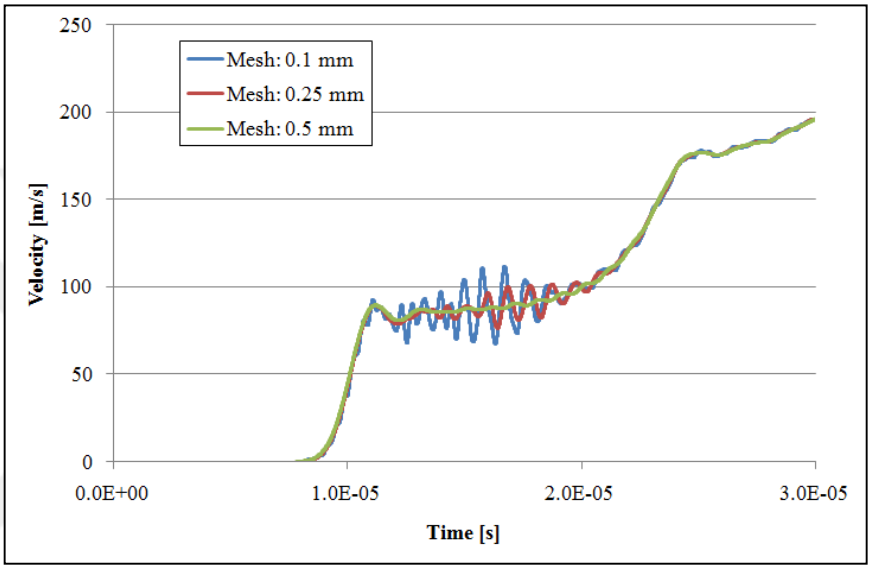

Figure 56 Mesh Size Effect on the Autodyn Simulations of Modified Taylor Impact Test

Figure 57 compares free surface velocities determined by Autodyn and by VISAR measurement. Test free surface velocity results are given in Figure 51 for the projectile having 180 m/s velocity. There are two different test results and both give the similar velocity profiles.

The comparison given in Figure 57 shows that there are slight differences between the simulation and test results. Velocity fluctuations occurring after the specimen reaches the final velocity are ignored since the relevant part of the velocity profile is the initial step until about 40 μs. The free surface velocity of the simulation is about 86 m/s and the free surface velocity obtained from the test is 71 m/s. As seen in Figure 57, there

is approximately 15 m/s shift between the free surface velocities obtained by the Modified Taylor Impact test and Autodyn simulation.

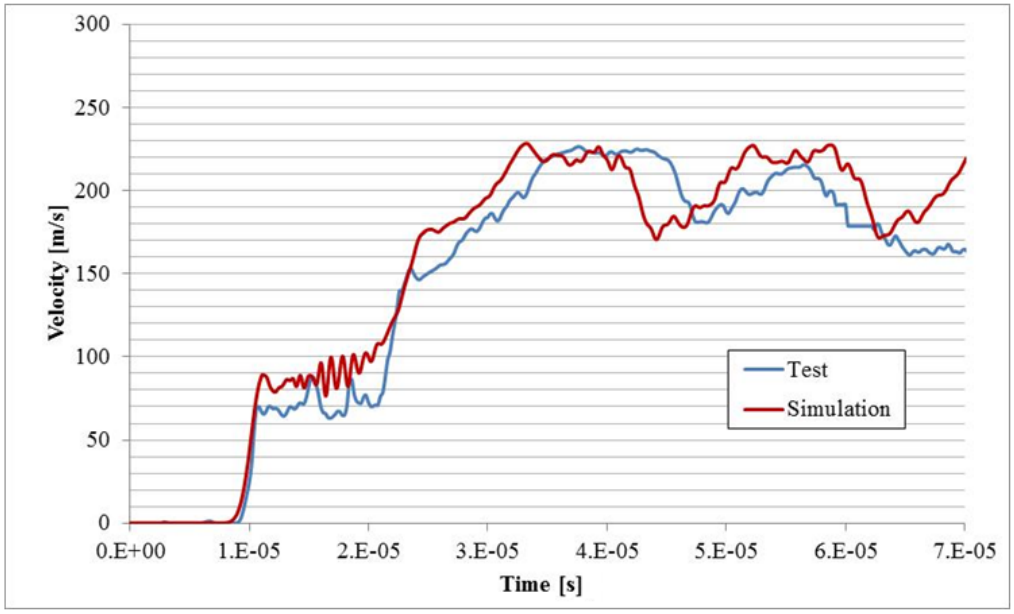

Figure 57 Comparison of Autodyn Simulations Conducted by Experimentally Determined Parameters and Test Results

It is noted that since in the Autodyn simulation, the parameters of the Johnson Cook model are taken from the modified impact test results performed, it is expected that test and simulation results would agree with each much better. The slight difference between the test and Autodyn simulations is mainly attributed to the VISAR measurements since the modified impact test was performed for the first time within the scope of this thesis study.

The final dimensions of the Autodyn analysis sample are also compared with the final dimensions of the test sample. In the simulation, the initial length is 50.03 mm and the initial diameter of the cylindrical bar is 5.09 mm. The deformed model has a final dimension of 47.53 mm length and final diameter of the impacted surface 5.72 mm, as shown in Figure 58.

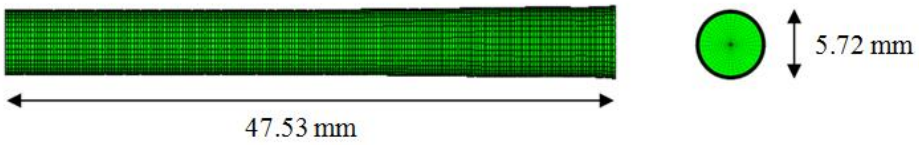

Figure 58 Dimensions of the Sample at the End of the Simulation

The changes in the dimensions of the test specimen and the simulated specimen are given in Table 9. As shown in the table, the length of the specimen decreased and the impact surface enlarged due to the plastic deformation. The non-impact surface diameter remains constant since the plastic waves could not reach this side of the sample. As shown in Table 9, the length and diameter changes are slightly different. They should be closer for an exactly defined model. However, this comparison is not reliable due the test results including bucklings.

Table 9 Initial and Final Dimensions of the Sample for both Test and Simulation

Results	Dimensions	Initial	Final	Change [%]
Test	Diameter [mm]	5.09	5.87	15.3%
Simulation	Diameter [mm]	5.09	5.72	12.4%
Test	Length [mm]	50.03	46.79	-6.5%
Simulation	Length [mm]	50.03	47.53	-5.0%

Al 7075-T651 material studied in dynamic loading conditions in this thesis was also studied in the literature with different Johnson-Cook parameters. Here, the results of Autodyn-2D analysis conducted with different Johnson-Cook parameters obtained from the literature for the same material Al 7075-T651 are compared with the present analysis and test results. For this purpose, parameters of the Johnson-Cook yield strength model of Al 7075-T651 obtained two different studies in the literature are used in Autodyn simulations ([23], [4]). Parameters of the Johnson-Cook strength

model determined experimentally in the thesis and those obtained from References [23] and [4] are given in Table 10.

Table 10 Johnson-Cook Parameters for the Al 7075-T651 Material

Reference Studies	Yield Strength, A [MPa]	Hardening Constant, B [MPa]	Hardening Exponent, n	Strain Rate Constant, C	Thermal Softening Exponent, m
Present Study	570	680	0.63	0.011	1.61
Reference 23	520	477	0.52	0.01	1.61
Reference 4	527	575	0.72	0.017	1.61

Autodyn simulations for the modified Taylor impact test are conducted utilizing the parameters of the Johnson-Cook yield strength model obtained from References [23] and [4] and free surface velocity profiles obtained from these analyses are compared with the free surface velocity profile obtained by Autodyn simulation utilizing the experimentally determined parameters of the Johnson-Cook yield strength model in Figure 59. Figure 59 shows good agreement between the free surface velocity profiles obtained by Autodyn simulations utilizing the parameters of the Johnson-Cook yield strength model from References [23] and [4]. However, free surface profile obtained by Autodyn simulation utilizing the experimentally determined Johnson-Cook parameters is slightly different from the free surface velocity profiles obtained by Autodyn simulations utilizing the parameters of the Johnson-Cook yield strength model from References [23] and [4]. But in the overall, present test and three analysis results agree with each other reasonably well. There might be some error in the test result due to some mis-tuned parameters in adjusting the VISAR system. It seems like if the test velocity profile is shifted up by some amount present test and analysis results would agree with each other much better.

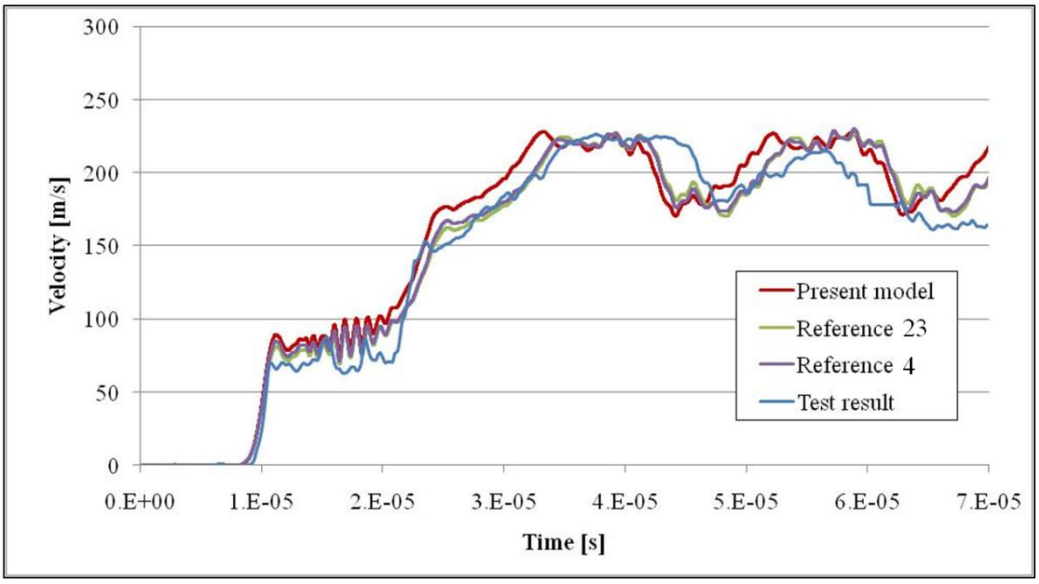

Figure 59 Comparison of Free Surface Velocities Determined by Autodyn Simulations Utilizing Experimentally Determined Johnson-Cook Parameters and Parameters from the Literature

It is to be noted that there are two ways to check the VISAR system measurements. One of them is to measure the free surface velocity by another system such as a high speed camera working in nanosecond time levels. Comparison of the results would give valuable information regarding the VISAR measurement. Another way is that experiments could be performed for different materials for which reliable material models are known, such as for copper. The second method seems more practical since it can be carried out by the existing tools.

CHAPTER 6

CONCLUSION

Hydrocodes are widely used to model dynamic events such as impact, penetration, and explosion. Autodyn is commercial hydrocode software widely used in the industry and for academic studies. To simulate the behaviour of any material in dynamic conditions in Autodyn or any other hydrocode, dynamic strength model of the material should be defined.

The models representing behavior of materials at high strain rates are called dynamic strength models. Dynamic strength models are used to characterize the mechanical behavior of materials under high loadings and high strain rates. Although characteristics of the most of the materials in quasi-static conditions are obtained from the literature or open sources or quasi-static testing, dynamic characteristics cannot be found easily. There are various material models such as Johnson-Cook, Zerilli-Amstrong, Mechanical Threshold, Steinberg-Lund, Preston-Tonks-Wallace etc. to model the dynamic behaviour of materials.

Johnson-Cook yield strength model is one of the simplest models of the dynamic strength models. According to the Johnson Cook material model, yield strength of a material depends on strain, strain rate and temperature. Johnson-Cook model is defined by five constants which are yield strength parameter *A*, hardening constant *B*, strain rate constant *C*, hardening exponent *n*, and thermal softening exponent *m*. In other material models, material behavior depends on more properties addition to the parameters of the Johnson-Cook model such as crystal structure type, grain size**,** melting, Bauschinger effect etc. However, parameters of these models are comparatively more difficult to determine than the parameters of the Johnson-Cook model. For most of the metallic materials such as steel, aluminum, copper, Johnson-Cook model gives highly accurate results. Since Al 7075-T651, which is a metallic material widely used in aerospace and defense industry, is investigated in this thesis,

Johnson-Cook model was preferred as the yield strength model. This thesis aims to determine the parameters *A*, *B*, *C* and *n* of the Johnson-Cook yield strength model experimentally and to verify the experimentally determined constants by simulating the Modified Taylor impact test in Autodyn.

Tensile test system was used in this study to determine the hardening constant *B*, and the hardening exponent *n* at a low strain rate which is assumed to be in the quasi-static range. Tensile test specimens are prepared according to ASTM E8M standard and true stress-true strain curves are obtained. True stress and strain curves are fitted to an equation expressed by *B*, and *n* constants in quasi-static condition, and hardening constant *B*, and the hardening exponent *n* are determined. To define the Johnson-Cook yield strength model, parameters *A* and *C* should also be determined.

Yield strength of a material in high strain rates can be determined by various methods such as drop weight tests, Split-Hopkinson bar tests, Taylor or modified Taylor impact tests. In this study, modified Taylor impact test system was preferred due to covering higher strain rates compared to others. Also, it is aimed to establish the modified Taylor impact test setup in TÜBİTAK SAGE to be used for other projects.

The test system composed of the modified Taylor impact test system and the VISAR is used to measure the free surface velocity of a specimen. VISAR is a measurement technique used with the modified Taylor impact test to obtain the free surface velocity of the samples. In the modified Taylor test system, a projectile impacts a long and thin specimen and the specimen begins to accelerate to the free-end side (to non-impacted side). This acceleration occurs due to elastic wave and the free-end side velocity increases at each reflection of elastic wave from surface. VISAR system sends a laser beam to the free surface of the specimen and by using the time lag in the reflected beam, VISAR measures the instantaneous surface velocity. Dimensions of the specimen are defined such that 1-D wave propagation assumption is used. The length of the specimen is ten times larger than the diameter thereby the distortional wave effects are neglected in the calculations.

Free surface velocity profile of the specimen made of Al 7075-T651 has an increase of the velocity step by step from the static position to the final velocity. By using this velocity profile, free surface velocity and the strain rate are determined. Free surface velocity, density and elastic wave speed are three properties affecting the yield stress of a specimen in high strain rates. Density and elastic wave speed can be found from the literature or the Al 7075-T651 material. By using the modified Taylor impact and VISAR test setup, free surface velocity and the strain rate that the material is exposed to are obtained and the yield stress is calculated in the measured strain rate range.

Establishing the test setup and performing successful measurements were most time consuming but at the same time the most significant part of the thesis. Firstly, VISAR system settings were studied. After having the VISAR system work, the test system was prepared including the gas gun and the target cabin.

In the laboratory, there is a single stage gas gun and a target cabin next to the exit side of the gas gun barrel. Inside the target cabin, firstly a velocity measurement system was placed very close to the exit of the gas gun barrel to measure the initial velocity of the projectile. Then, a metallic wall, which had a hole for the test sample and sample holder foam, was fixed inside the cabin. The projectile impacted the sample and two specimens flew through the VISAR measurement system located at the end of the cabin. To prevent the damages of the specimens on the very sensitive VISAR system, another steel wall was fixed to the cabin floor. This wall has a hole large enough for the laser beam to pass through, but narrow enough so that the specimens could not pass through. Also, an additional protective case was manufactured for the VISAR optic tools against the ricochets of the particles.

In this study, Johnson-Cook parameters of Al 7075-T651 are obtained by the modified Impact test and verified by Autodyn-2D simulations. Modified Taylor impact test is simulated by a steel projectile having a certain velocity and a static sample modeled by the Johnson-Cook yield strength model utilizing the parameters obtained in the experiments performed. A gauge point is fixed to the free end of the sample to record the velocity change. Although the free surface velocity profiles obtained by the

Autodyn analysis is similar with the test results, they do not have perfect agreement. The analyses are repeated by two different models of the same material taken from the literature and it is seen that they gave better results than the present study. Therefore, it s concluded that either the parameters of the Johnson-Cook yield strength model are a little off or the free surface velocity profile determined by the VISAR measurement has some error. Since the VISAR system is used for the first time within the scope of the present thesis study, it is considered that the system still needs some tuning to properly measure the free surface velocity. As for the parameters of the Johnson-Cook yield strength model, yield strength parameter *A* and hardening constant *B* are higher than the corresponding values found in the literature for the same material. Therefore, as a future study both the tensile and modified Taylor impact tests can be repeated to determine the parameters *A* and *B* again. As a matter of fact, according to the tensile test standards, a minimum of five tests have to be performed and average of the five tests has to be reported as the result of the tensile test. Considering the difficulty of obtaining reliable data in VISAR measurements, more modified Taylor impact tests have to be performed to have reliable prediction of the free surface velocity profile. Moreover, in the future, the test methodology can be applied for other metallic material such as OFHC copper for which the parameters of the Johnson-Cook material model are known to a higher degree of accuracy since they are studied more frequently in the literature. If materials with more reliable parameters of the Johnson-Cook yield strength model are tested utilizing the test procedure described in the thesis, then the VISAR system measurements can be improved based on the comparison test data and the hydrocode simulations.

This study was conducted for a specific material but the methodology can be applied to obtain the parameters of the Johnson-Cook yield strength model for any other metallic materials. Although the strength properties of common materials like aluminum, steel, copper can be obtained from the literature, the properties of most of the materials used in the defense industry like tungsten alloys or certain aluminum alloys and steels may not be obtained easily. This system provides to obtain dynamic models of any metallic material.

In the future studies, the thermal softening parameter *m* maybe also obtained by using tensile tests in different temperatures. This method needs very controllable test setup and measurements. Also, higher strain rates may be reached by using the same test system in a different method which is known as planar-plate impact test. Instead of using a long and small diameter specimen, very thin and large diameter specimen is used in the planar-plate impact tests. In the planar-plate impact tests, higher strain rates can be reached in the range of 10^5-10^6 s^{-1}.The experiments conducted at different strain rates increases the reliability of the dynamic model since there will be more verified data. Johnson-Cook yield strength model gives a linear relation between the stress and the strain rate in logarithmic scale. However, if the confirmed data is obtained for more than two data points, different linear relations can be defined between each pair of data points. By this way, a discrete model can be obtained yielding higher accuracy in the simulations.

REFERENCES

[1] ANSYS Autodyn, version 16.2.

[2] ASTM Standard E8M, (2009). Standard Test Methods for Tension Testing of Metallic Materials, ASTM International, West Conshohocken, PA, 2009.

[3] Barker L. M. and Hollenbach R. E. (1972). Laser interferometer for measuring high velocities of any reflecting surface. *Journal of Applied Physics*, 43 (11):4669.

[4] Brar, N., Joshi, V., and Harris, B., (2009). Constitutive Model Constants for Al 7075-T651 and Al 7075-T6, 16th APS Topical Conference on Shock Compression of Condensed Matter, *American Physical Society*, Nashville, TN.

[5] Bunch, B. (2004).The history of science and technology. Boston: Houghton Mifflin Company.

[6] Chen, V. (2011).The Micro-Doppler effect in radar. Boston: Artech House.

[7] Chhabildas, L. (2005). High pressure shock compression of solids the science and technology of high-velocity impact. New York: Springer.

[8] Collins, G., S., (2002). An introduction to Hydrocode.

[9] Davies, R. (1948). A Critical Study of the Hopkinson Pressure Bar.*Philosophical Transactions of the Royal Society A: Mathematical, Physical and Engineering Sciences,* 375-457.

[10] Ferranti, L. J. (2007). Mechanochemical reactions and strengthening in epoxy-cast aluminum iron-oxide mixtures. PhD's thesis, Georgia Institute of Technology, 2007, pp. 146-157. *School of Materials Science and Engineering*.

[11] Follansbee, P., & Kocks, U. (1986). A constitutive description of the deformation of copper based on the use of the mechanical threshold stress as an internal state variable. Acta Metallurgica, 81-93.

[12] Forde, L., Proud, W., & Walley, S. (2009). Symmetrical Taylor impact studies of copper. Proceedings of the Royal Society A: Mathematical, Physical and Engineering Sciences, 465(2103), 769-790.

[13] Gama, B., Lopatnikov, S., & Gillespie, J. (2004). Hopkinson bar experimental technique: A critical review. *Applied Mechanics Reviews*,*57*(4), 223-250.

[14] Goto, D.M., Bingert, J.F., Reed, W.R., Garrett, R.K., 2000b. Anisotropy-corrected MTS constitutive strength modeling in HY-100 steel. Scr. Mater. 42, 1125–1131.

[15] Hariharan, P. (2007). *Basics of interferometry*. Amsterdam: Elsevier Academic Press.

[16] Hazell P. J. (2015). Armour: Materials, Theory and Design. CRC Press.

[17] Hiermaier, S. (2008).Structures under crash and impact continuum mechanics, discretization and experimental characterization. New York: Springer.

[18] Holtkamp, D. (2008). Survey of optical velocimetry experiments – applications of PDV, a heterodyne velocimeter. *Los Alamos National Laboratory*.119-128.

[19] Hopkinson, B. (1914). A Method of Measuring the Pressure Produced in the Detonation of High Explosives or by the Impact of Bullets. *Philosophical Transactions of the Royal Society A: Mathematical, Physical and Engineering Sciences*, 437-456.

[20] Huang, S., Xia, K., & Dai, F. (2011). A Dynamic Punch Method to Quantify the Dynamic Shear Strength of Brittle Solids. *Dynamic Behavior of Materials, Volume 1 Conference Proceedings of the Society for Experimental Mechanics Series*, 157-163.

[21] ISO Standard 6892, 2009, Metallic Materials Tensile Testing, International Standard.

[22] Johnson, G., R., & Cook, W., H., (1983). A constitutive model and data for metals subjected to large strains, high strain rates and high temperatures. *Proceedings of Seventh International Symposium on Ballistics*, The Hague, The Netherlands, 541-547.

[23] Jorgensen K. C. (2014). Modeling of Armor-piercing Projectile Perforation of Thick Aluminium Plates. 13th International LS-DYNA Users Conference.

[24] Karman T. v. and Duwez P., (1950). The Propagation of Plastic Deformation in Solids. *Journal of Applied Physics* **21**, 987-994.

[25] Kessler, M. (2004).Advanced topics in characterization of composites. Victoria, B.C.: Trafford.

[26] Khan, A., & Huang, S. (1995).Continuum theory of plasticity. New York: Wiley.

[27] Kolsky, H. (1949). An Investigation of the Mechanical Properties of Materials at very High Rates of Loading. *Proceedings of the Physical Society. Section B,* 676-700.

[28] Kolsky, H. (1963).Stress waves in solids. New York: Dover Publications.

[29] Konokman, H.E., (2008). Development of Lagrangian Hydrocode for High Speed Impact Analysis and Its Experimental Verification. Master of Science's thesis, Middle East Technical University, 2008.

[30] Lianis, G., & Ford, H. (1957). An experimental investigation of the yield criterion and the stress-strain law. *Journal of the Mechanics and Physics of Solids,5*, 215-222.

[31] Lode, W. (1925). Versucheüber den Einfluss der mittlerenHauptspannung auf die Fliessgranze. *Z. Angew. Math.Mech.*

[32] Lubliner, J. (1990).Plasticity theory. New York: Macmillan

[33] Martin, Froeschner & Associates User Manual.

[34] Meyers, M. (1994).Dynamic behavior of materials. New York: Wiley.

[35] Nishida, E. E. (2010). Distinguishing inertia effects from the intrinsic mechanical behavior of soft materials at high strain rates by Kolsky bar experiments (Master's thesis, Purdue University, 2010) (p. 12). Ann Arbor: ProQuest LLC.

[36] Preston, D., Tonks, D., & Wallace, D. (2002). Model of plastic deformation for extreme loading conditions. *Journal of Applied Physics*, 211-220.

[37] Proulx, T. (2011). A Dynamic Punch Method to Quantify the Dynamic Shear Strength of Brittle Solids. In Dynamic behavior of materials proceedings of the 2010 Annual Conference on Experimental and Applied Mechanics. New York: Springer.

[38] Rohr, I., Nahme, H., & Thoma, K. (2003). A modified TAYLOR-test in combination with numerical simulations - a new approach for the determination of model parameters under dynamic loads. *Journal De Physique IV (Proceedings)*, 513-518.

[39] Rohr, I., Nahme, H., &Thoma, K. (2005). Material characterization and constitutive modelling of ductile high strength steel for a wide range of strain rates. *International Journal of Impact Engineering*, 401-433.

[40] Rohr, I., Nahme, H., & Thoma, K. (2008). Material characterization and constitutive modeling of a tungsten-sintered alloy for a wide range of strain rates. International Journal of Impact Engineering, 811-819.

[41] Rosenberg, Z., & Dekel, E. (2012). Terminal ballistics. Berlin: Springer.

[42] Rydin, R. W. (1996). *Using The Drop Weight Impact Tower To Assess Impact Resistance O F Frp Composite Plates* (Doctor of Philosophy's thesis, Faculty of the University of Delaware, 1996) (p. 44). MI: UMI Company.

[43] Starr, C., & Alcock, J. (1991). Biology: Concepts and applications. Belmont, Calif.: Wadsworth Pub.

[44] Steel, W. (1967). Interferometry. London: Cambridge U.P.

[45] Steinberg, D., & Lund, C. (1988). A constitutive model for strain rates from 10^{-4} to 10^{-6} s^{-1}.*Journal of Applied Physics*,1528-1533.

[46] Strand, O., Goosman, D., Martinez, C., Whitworth, T., & Kuhlow, W. (2006). Compact system for high-speed velocimetry using heterodyne techniques. *Review of Scientific Instruments, 77*, 083108, 1-7.

[47] Taylor, G. (1931). The Use of Flat-Ended Projectiles for Determining Dynamic Yield Stress. I. Theoretical Considerations. Proceedings of the Royal Society A: *Mathematical, Physical and Engineering Sciences*, 289-299.

[48] Taylor, G. I., and Quinney H. (1931). The plastic distortion of metals. *Phil. Trans. R. Soc*., London.

[49] Walley, S.M., Field, J.E. (2005).Elastic Wave Propagation in Materials. *Encyclopedia of Materials: Science and Technology*. Elsevier

[50] Wasley, R. J. (1973). Stress Wave Propagation in Solids: An Introduction. Marcel Dekker, Inc.

[51] Wilkins M. L. and Guinan M. W.(1973). Impact of Cylinders on a Rigid Boundary. *J. Appl. Phys.* 44, 1200-1206.

[52] Yavuz, M. S., (2011). Numerical and Experimental Investigation of Jet Formation and Particulation in Shaped Charges with Tulip-Like Steel Liners. Master of Science thesis, Middle East Technical University, 2011.

[53] Zerilli, F., J., & Amstrong, R., W., (1987). Dislocation mechanics based constitutive relations for material dynamics calculations. *Journal of Applied Physics*, 1816-1825.

[54] Zhuang, S. (2002). *Shock wave propagation in periodically layered composites*. PhD's thesis, California Institute of Technology, 2002. (pp. C6-C10). MI: UMI Company.

[55] Zukas, J. (2004). Introduction to hydrocodes. Amsterdam: Elsevier.

[56] Zukas, J. (1982). Impact dynamics. New York: Wiley.